

# Predicting Frictional Properties of Graphene Kirigami Using Molecular Dynamics and Neural Networks

*Designs for a negative friction coefficient*

Mikkel Metzsch Jensen



Thesis submitted for the degree of  
Master in Computational Science: Materials Science  
60 credits

Department of Physics  
Faculty of mathematics and natural sciences

UNIVERSITY OF OSLO

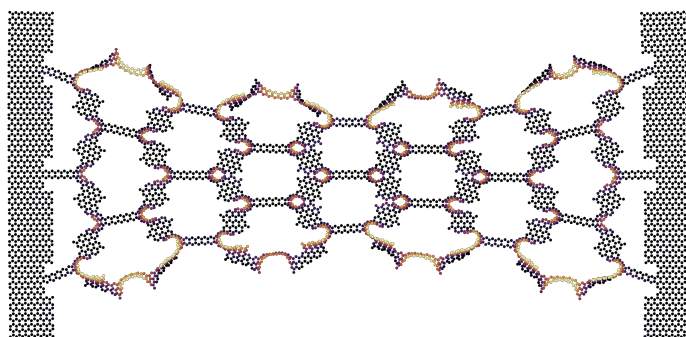
Spring 2023



# Predicting Frictional Properties of Graphene Kirigami Using Molecular Dynamics and Neural Networks

*Designs for a negative friction coefficient*

Mikkel Metzsch Jensen





© 2023 Mikkel Metzsch Jensen

Predicting Frictional Properties of Graphene Kirigami Using Molecular Dynamics and Neural Networks

<http://www.duo.uio.no/>

Printed: Reprosentralen, University of Oslo

# Abstract

Various theoretical models and experimental results propose different governing mechanisms for friction at the nanoscale. We consider a graphene sheet modified with Kirigami-inspired cuts and under the influence of strain. Prior research has demonstrated that this system exhibits out-of-plane buckling, which could result in a decrease in contact area when sliding on a substrate. According to asperity theory, this decrease in contact area is expected to lead to a reduction of friction. However, to the best of our knowledge, no previous studies have investigated the friction behavior of a nanoscale Kirigami graphene sheet under strain. Here we show that specific Kirigami designs yield a non-linear dependency between kinetic friction and the strain of the sheet. Using molecular dynamics simulations, we have found a non-monotonic increase in friction with strain. We found that the friction-strain relationship does not show any clear dependency on contact area which contradicts asperity theory. Our findings suggest that the effect is associated with the out-of-plane buckling of the graphene sheet and we attribute this to a commensurability effect. By mimicking a load-strain coupling through tension, we were able to utilize this effect to demonstrate a negative friction coefficient on the order of  $-0.3$  for loads in the range of a few nN. In addition, we have attempted to use machine learning to capture the relationship between Kirigami designs, load, and strain, with the objective of performing an accelerated search for new designs. Although this approach yielded some promising results, we conclude that further improvements to the dataset are necessary in order to develop a reliable model. We anticipate our findings to be a starting point for further investigations of the underlying mechanism for the frictional behavior of a Kirigami sheet. For instance, the commensurability hypothesis could be examined by varying the sliding angle in simulations. We propose to use an active learning strategy to extend the dataset for the use of machine learning to assist these investigations. If successful, further studies can be done on the method of inverse design. In summary, our findings suggest that the application of nanoscale Kirigami can be promising for developing novel friction-control strategies.



# Acknowledgments

The task of writing a master’s thesis is a demanding and extensive project which I could not have done without the support of many good people around me. First of all, I want to thank my supervisors Henrik Andersen Sveinsson and Anders Malthe-Sørenssen for the assistance in this thesis work. I am especially grateful for the weekly meetings with Henrik and the inspiring discussions had as we unraveled the discoveries related to the topic of this thesis. I remember that I initially asked for an estimate of how much time he had available for supervision and the answer was something along the lines of “There are no limits really, just send me an email and we figure it out”. This attitude captures the main experience I have had working with Henrik and I am profoundly grateful for the time and effort he has put into this project. I hope that he did not regret this initial statement too much, because I have certainly been taken advantage of it. I also want to thank Even Marius Nordhagen for technical support regarding the use of the computational cluster. In that context, I also want to acknowledge the Center for Computing in Science Education (CCSE) for making these resources available.

I would like to express my gratitude to all the parties involved in making it possible for me to write my thesis from Italy. I am particularly grateful for the flexibility shown by my supervisors and for the support of Anders Kvellestad, who allowed me to work remotely as a group teacher. I would also like to thank Scuola Normale Superiore for providing me with access to their library.

I realize that it is a commonly used cliché to express gratitude for the support of loved ones. However, I want to highlight the exceptional role played by my fiancé, Ida, who deserves the main credit for enabling me to maintain a healthy state of mind. She has provided me with a solid foundation for a fulfilling life that enables me to pursue secondary objectives, such as an academic career. I look forward to spending the rest of my life with you.

In this thesis, I have used the formal pronoun “we” mainly as a customary habit related to the formalities of scientific writing in a team. Nonetheless, I have realized that this usage is more fitting as I have not been working alone on this project. I have received support all the way from colleagues and friends at the University of Oslo, my family residing in Denmark, and my life partner who slept beside me every night here in Italy. They are the “good people around me” who have made this thesis possible.





# Acronyms

**CM** Center of Mass. 13, 14

**GAN** Generative Adversarial Networks. 2

**LJ** Lennard-Jones. 17, 18

**MD** Molecular Dynamics. 1, 2, 3, 4, 9, 10, 20, 22

**ML** Machine Learning. 2, 10

**std** Standard Deviation. 15, 16, 19, 20



# Contents

<b>1</b>	<b>Introduction</b>	<b>1</b>
1.1	Motivation . . . . .	1
1.2	Goals . . . . .	2
1.3	Contributions . . . . .	3
1.4	Thesis structure . . . . .	3
<b>I</b>	<b>Background Theory</b>	<b>5</b>
<b>II</b>	<b>Simulations</b>	<b>7</b>
<b>2</b>	<b>Pilot study</b>	<b>9</b>
2.1	Friction simulation parameters . . . . .	9
2.2	Force traces . . . . .	9
2.2.1	Force oscillations . . . . .	9
2.2.2	Decompositions . . . . .	13
2.2.3	Center of mass path . . . . .	13
2.3	Defining metrics for friction . . . . .	15
2.3.1	Kinetic friction . . . . .	15
2.3.2	Static friction . . . . .	16
2.4	Out-of-plane buckling . . . . .	16
2.5	Investigating default parameters . . . . .	19
2.5.1	Computational cost . . . . .	20
2.6	Strain and load dependencies . . . . .	22
2.6.1	Pressure reference for normal load . . . . .	22
2.6.2	Strain dependency . . . . .	22
2.6.3	Load dependency . . . . .	24
2.6.4	Prospects for achieving a negative friction coefficient . . . . .	27
	<b>Appendices</b>	<b>29</b>



# Chapter 1

## Introduction

### 1.1 Motivation

Friction is the force that prevents the relative motion of objects in contact. In our everyday life, we recognize it as the inherent resistance to sliding motion. Some surfaces appear slippery and some appear rough, and we know intuitively that sliding down a snow-covered hill is much more exciting than its grassy counterpart. Without friction, it would not be possible to walk across a flat surface, lean against the wall without falling over or secure an object by the use of nails or screws [1, p. 5]. It is probably safe to say that the concept of friction is integrated into our everyday life to such an extent that most people take it for granted. However, the efforts to control friction date back to the early civilization (3500 B.C.) with the use of the wheel and lubricants to reduce friction in translational motion [2]. Today, friction is considered a part of the wider field *tribology* derived from the Greek word *tribos* meaning “rubbing”. It includes the science of friction, wear and lubrication [2]. The most compelling motivation to study tribology is ultimately to gain full control of friction and wear for various technical applications. Especially, the reduction of friction is of great interest since this can be utilized to improve energy efficiency in mechanical systems with moving parts. Hence, it has been reported that tribological problems have a significant potential for both economic and environmental improvements [3]:

“On global scale, these savings would amount to 1.4% of the GDP annually and 8.7% of the total energy consumption in the long term.” [4].

On the other hand, the reduction of friction is not the only sensible application for tribological studies. Controlling frictional properties, besides minimization, might be of interest in the development of a grasping robot where finetuned object handling is required. While achieving a certain “constant” friction response is readily obtained through appropriate material choices, we are yet to unlock the full capabilities to alter friction dynamically on the go. One example from nature inspiring us to think along these lines is the gecko feet. More precisely, the Tokay gecko has received a lot of attention in scientific studies aiming to unravel the underlying mechanism of its “toggleable” adhesion properties. Although the gecko can produce large adhesive forces, it retains the ability to remove its feet from an attachment surface at will [5]. This makes the gecko able to achieve a high adhesion on the feet when climbing a vertical surface while lifting them for the next step remains relatively effortless. For a grasping robot, we might consider an analog frictional concept of a surface material that can change from slippery to rough on demand depending on specific tasks; slippery and smooth when interacting with people and rough and firmly gripping when moving heavy objects.

In recent years an increasing amount of interest has gone into the studies of the microscopic origins of friction, due to the increased possibilities in surface preparation and the development of nanoscale experimental methods. Nano-friction is also of great concern for the field of nano-machining where the frictional properties between the tool and the workpiece dictate machining characteristics [3]. With concurrent progress in computational capacity and development of Molecular Dynamics (MD), numerical investigations serve as an invaluable tool for getting insight into the nanoscale mechanics associated with friction. This simulation-based approach can be considered as a “numerical experiment” enabling us to create and probe a variety of high-complexity systems which are still out of reach for modern experimental methods.

In materials science such MD-based numerical studies have been used to explore the concept of so-called *metamaterials* where the material compositions are designed meticulously to enhance certain physical properties [6–11]. This is often achieved either by intertwining different material types or removing certain regions completely. In recent papers by Hanakata et al. [6, 7], numerical studies have showcased that the mechanical properties of a graphene sheet, yield stress and yield strain, can be altered through the introduction of so-called *Kirigami* inspired cuts into the sheet. Kirigami is a variation of origami where the paper is cut additionally to being folded. While these methods originate as an art form, aiming to produce various artistic objects, they have proven to be applicable in a wide range of fields such as optics, physics, biology, chemistry and engineering [12]. Various forms of stimuli enable direct 2D to 3D transformations through the folding, bending, and twisting of microstructures. While original human designs have contributed to specific scientific applications in the past, the future of this field is highly driven by the question of how to generate new designs optimized for certain physical properties. However, the complexity of such systems and the associated design space makes for seemingly intractable<sup>1</sup> problems ruling out analytic solutions.

Earlier design approaches such as bioinspiration, looking at gecko feet for instance, and Edisonian, based on trial and error, generally rely on prior knowledge and an experienced designer [9]. While the Edisonian approach is certainly more feasible through numerical studies than real-world experiments, the number of combinations in the design space rather quickly becomes too large for a systematic search, even when considering the computation time on modern-day hardware. However, this computational time constraint can be relaxed by the use of machine learning (ML) which has been proven successful in the establishment of a mapping from the design space to physical properties of interest. This gives rise to two new styles of design approaches: One, by utilizing the prediction from a trained network we can skip the MD simulations altogether resulting in an *accelerated search* of designs. This can be further improved by guiding the search according to the most promising candidates. For instance, as done with the *genetic algorithm* based on mutation and crossing. Another more sophisticated approach is through generative methods such as *Generative Adversarial Networks* (GAN) or diffusion models. The latter is being used in state-of-the-art AI systems such as OpenAI’s DALL-E2 [13] or Midjourney [14]. By working with a so-called *encoder-decoder* network structure, one can build a model that reverses the prediction process. This is often referred to as *inverse design*, where the model predicts a design based on physical target properties. In the papers by Hanakata et al. [6, 7] both the accelerated search and the inverse design approach was proven successful to create novel metamaterial Kirigami designs with the graphene sheet.

Hanakata et al. attribute the variation in mechanical properties to the non-linear effects arising from the out-of-plane buckling of the sheet. Since it is generally accepted that the surface roughness is of great importance for frictional properties it can be hypothesized that Kirigami-induced out-of-plane buckling can also be exploited for the design of frictional metamaterials. For certain designs, we might hope to find a relationship between the stretching of the sheet and frictional properties. If significant, this could give rise to an adjustable friction beyond the point of manufacturing. For instance, the grasping robot might apply such a material as artificial skin for which stretching or relaxing of the surface could result in a changeable friction strength.

In addition, the Kirigami graphene properties can be explored through a potential coupling between the strain and the normal load, through a nanomachine design, with the aim of altering the friction coefficient. This invites the idea of non-linear friction coefficients which might in principle also take on negative values. This would constitute a rarely found property which is mainly observed for the unloading phase of adhesive surfaces [15] or in the loading phase of particular heterojunction materials [16, 17].

To the best of our knowledge, Kirigami has not yet been implemented to alter the frictional properties of a nanoscale system. However, in a recent paper by Liefferink et al. [18] it is reported that macroscale Kirigami can be used to dynamically control the macroscale roughness of a surface through stretching. They reported that the roughness change led to a changeable frictional coefficient by more than one order of magnitude. This supports the idea that Kirigami designs can be used to alter friction, but we believe that taking this concept to the nanoscale would involve a different set of governing mechanisms and thus contribute to new insight in this field.

## 1.2 Goals

In this thesis, we investigate the prospects of altering the frictional properties of a graphene sheet through the application of Kirigami-inspired cuts and stretching of the sheet. With the use of molecular dynamics (MD)

---

<sup>1</sup>In computer science we define an *intractable* problem as a problem with no *efficient* algorithm to solve it nor any analytical solutions. The only way to solve such problems is the *brute-force* approach, simply trying all possible combinations, which is often beyond the capabilities of computational resources.

simulations, we evaluate the frictional properties of various Kirigami designs under different physical conditions. Based on the MD results, we investigate the possibility to use machine learning for the prediction of frictional properties and subsequently using the model for an accelerated search of new designs. The main goals of the thesis can be summarized as follows.

1. Design an MD simulation procedure to evaluate the frictional properties of a Kirigami graphene sheet under specified physical conditions.
2. Develop a numerical tool to generate various Kirigami designs, both by seeking inspiration from macroscale designs and by the use of a random-walk-based algorithm.
3. Investigate the frictional behavior under varying strain and load for different Kirigami designs.
4. Develop and train a machine learning model to predict the MD simulation results and perform an accelerated search of new designs with the goal of optimizing certain frictional properties.

### 1.3 Contributions

By working towards the goals outlined above (Sec. 1.2), I have discovered a non-linear relationship between the kinetic friction and the strain for certain Kirigami patterns. This phenomenon was found to be associated with the out-of-plane buckling of the Kirigami sheet but with no clear relationship to the contact area or the tension in the sheet. I found that this method does not provide any mechanism for a reduction in friction, in comparison to a non-cut sheet. However, the straining of certain Kirigami sheets allows for a non-monotonic increase in friction. The relationship to normal load was proven negligible in this context and I have demonstrated that a coupled system of load and strain (through sheet tension) can exhibit a negative friction coefficient in certain load ranges. Moreover, I have created a dataset of roughly 10,000 data points for assessing the employment of machine learning and accelerated search of Kirigami designs. I have found, that this approach might be useful, but that it requires an extended dataset in order to produce reliable results for a search of new designs.

During my investigations, I have built three numerical tools, in addition to the usual scripts for data analysis, which are available on Github [19]. The tools are summarized in the following.

- I have written a LAMMPS-based [20] tool for simulating and measuring the frictional properties of a graphene sheet sliding on a substrate. The code is generally made flexible with regard to the choice of sheet configuration, system size, simulation parameters and MD potentials, which makes it applicable for further studies on this topic. I have also built an automatized procedure to carry out multiple simulations under varying parameters by submitting jobs to a computational cluster via an ssh connection. This was done by adding minor additions to the Python package developed by E. M. Nordhagen [21].
- I have generated a Python-based tool for generating Kirigami patterns and exporting these in a compatible format with the simulation software created. The generation of molecular structures is done with the use of ASE [22]. Our software includes two classes of patterns inspired by macroscale designs and a random walk algorithm which allows for a variety of different designs through user-defined biases and constraints. Given our system size of choice, the first two pattern generators are capable of generating on the order of  $10^8$  unique designs while the random walk generator allows for significantly more.
- I have built a machine-learning tool based on Pytorch [23] which includes setting up the data loaders, a convolutional network architecture, a loss function, and general algorithms for training and validating the results. Additionally, I have written several scripts for performing grid searches and analyzing the model predictions in the context of the frictional properties of graphene.

All numerical implementations have been originally developed for this thesis except for the libraries mentioned above along with common Python libraries such as Numpy and Matplotlib.

### 1.4 Thesis structure

The thesis is divided into two parts. In Part I we introduce the relevant theoretical background, and in Part II we present the numerical implementations and the results of this thesis.



Part **I** contains a description of the theoretical background related to Friction (??), Molecular Dynamics (??) and Machine Learning (??). In ?? we formulate our research questions in the light of the friction theory.

In Part **II**, we begin by presenting the system in ?? which includes a definition of the main parts of the system and the numerical procedures related to the MD simulation. Here we also present the generation of Kirigami designs. In Chapter 2 we carry out a pilot study where we evaluate the simulation results for various physical conditions and compare a non-cut sheet to two different Kirigami designs. In ??, we further explore the Kirigami patterns through the creation of a dataset and the employment of machine learning and an accelerated search for new designs. In ??, we use the results from the pilot study to demonstrate the possibility to achieve a negative friction coefficient for a system with coupled load and strain. Finally, in ??, we summarize our results and provide an outlook for further studies. Additional figures are shown in ??, ?? and ??.

**Part I**

**Background Theory**



# Part II

## Simulations



# Chapter 2

## Pilot study

In this chapter, we begin by analyzing the frictional properties of our system. Initially, we examine the results for a non-cut sheet to establish suitable metrics for a numerical evaluation of friction and validate our parameter choices. This provides a basis for the following study where we explore the frictional properties of the Tetrahedron and Honeycomb Kirigami patterns. We conduct a more thorough investigation of the friction dependencies to temperature, sliding speed, spring constant, and timestep. Finally, we investigate the kinetic friction across all three configurations when subjected to strain, including an examination of the relationship to contact area and the friction-load curves.

### 2.1 Friction simulation parameters

The MD simulations we will carry out to measure friction are governed by a small set of parameters. Since we aim to develop a machine-learning model, it is necessary to standardize these parameters. Therefore, we keep the majority of the parameters constant and only modify a small subset of them, which includes sheet configuration, strain, and load. Instead of starting with the parameter selection process, we first state the final choice in Table 2.1. Due to the great number of parameters, we did not make an exhaustive search of all parameters before deciding on the final choice. Instead, we have taken a basis in parameters used in similar friction simulations [24–28] and adjusted accordingly to the aim of getting stable measurements and reducing computation time where possible. Parameters such as initial relaxation time, pauses and strain speed are chosen mainly from the results of initial stability tests. That is, we visually verify that the system is close to an equilibrium state and that it does not carry momentum before going to the next step in the numerical procedure. The sheet and pull block sizes are chosen with a consideration of the balance between Kirigami design options and computational resources. The scan direction is selected to be parallel with the connecting line between the pull blocks. This choice is made primarily to minimize the complexity of the motion, as it is hypothesized that other scan directions might cause the center of the sheet to lag behind in the sliding motion and produce a slight side flexion. The remaining parameters: Temperature  $T$ , sliding speed  $v$ , spring constant  $K$ , normal load  $F_N$ , timestep  $dt$  and sliding distance have mainly been chosen because the friction output remains relatively stable with moderate perturbations around these default values. However, we will explain the parameter choices in more detail throughout this chapter. Note that the default values in Table 2.1 will be used when nothing else is stated explicitly.

### 2.2 Force traces

We begin by assessing the friction force traces, i.e. force vs. time curves, for a single friction simulation using the default parameters shown in Table 2.1 for a non-cut sheet with no strain applied and a normal load of 1 nN.

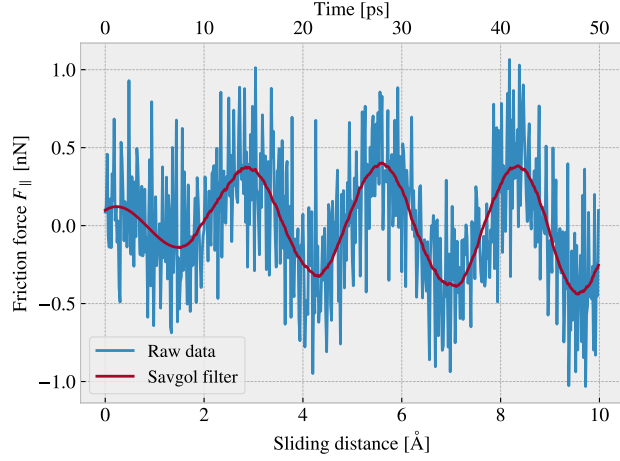
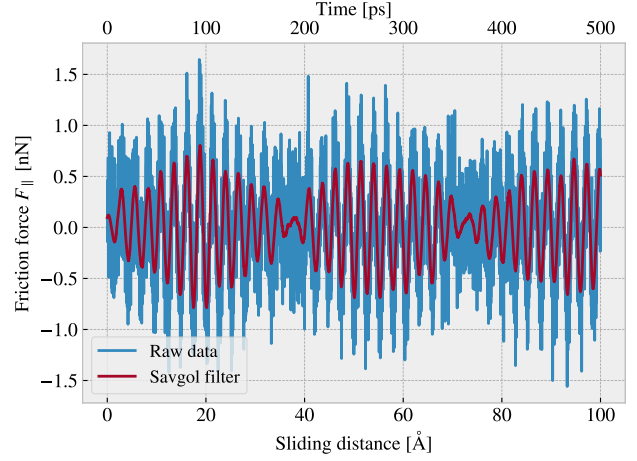
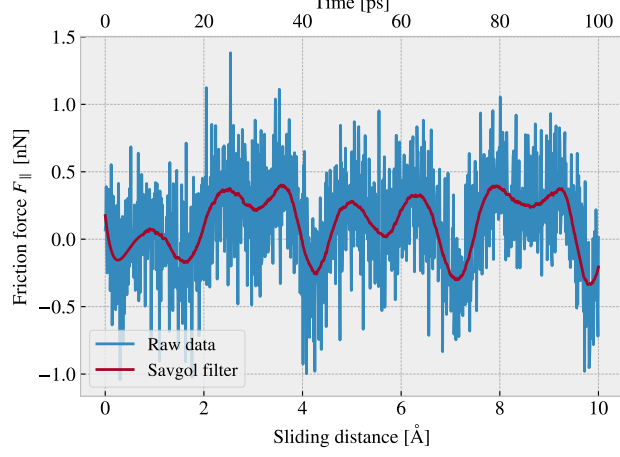
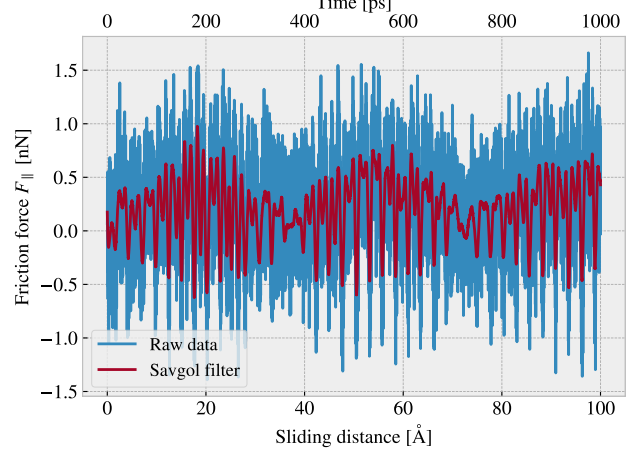
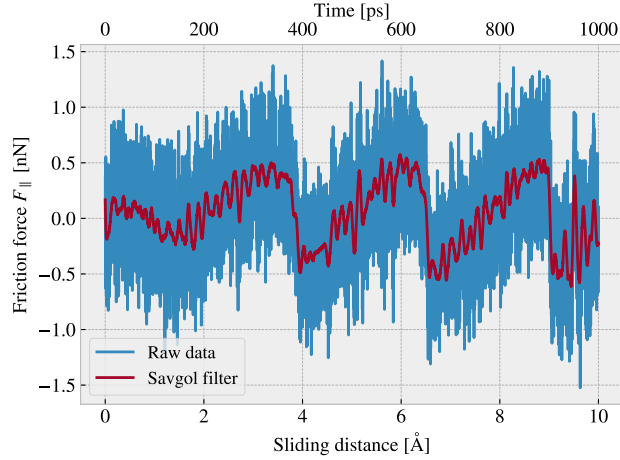
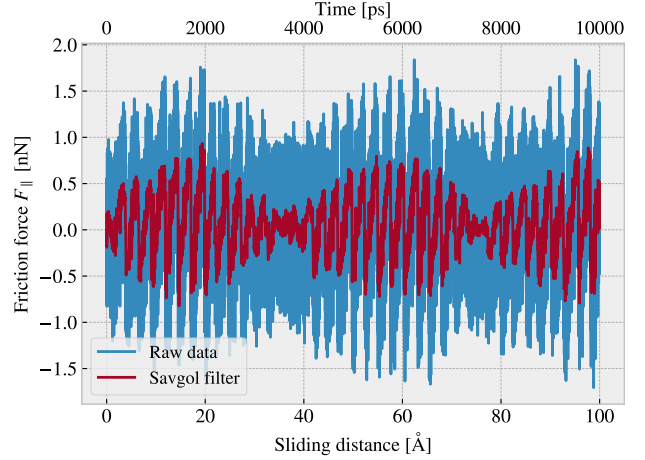
#### 2.2.1 Force oscillations

We evaluate the friction force as the force acting on the sheet from the substrate. We consider initially the force component  $F_{\parallel}$  parallel to the sliding direction shown in Fig. 2.1. We use a sample rate of  $10\text{ ps}^{-1}$  corresponding

**Table 2.1:** Parameters involved in the numerical MD simulation for measuring friction. The default values correspond to the final choice used for the ML dataset for which the shaded cells denote the parameters varied.

Parameter	Default value	Description
$T$	300 K	Temperature of the system.
$v$	20 m/s	Sliding speed for the sheet.
$K$	$\infty$	Spring constant for the coupling between the virtual atom and the sheet pull blocks.
Scan direction	$(x, y) = (0, 1)$ (zigzag direction)	The direction of sliding.
Sheet configuration	Contiguous	Binary mapping describing which atoms are removed (0) and which are still present (1) in the graphene sheet.
Strain amount	[0, rupture]	The ratio of change in length to the original length.
$F_N$	[0.1, 10] nN	Applied normal load to the pull blocks.
$dt$	1 fs	MD integration timestep.
Initial relaxation time	15 ps	Initial relaxation time before straining.
Pauses	5 ps	Relaxation pauses after strain, and during the normal load phase (before sliding).
Strain Speed	$0.01 \text{ ps}^{-1}$	The rate of straining for the sheet.
Slide distance	400 Å	How far the sheet is slid.
Sheet size	$130.029 \times 163.219 \text{ Å}$	Spatial 2D size of the sheet.
Pull block size	$2 \times 130.029 \times 15.183 \text{ Å}$	Spatial 2D size of the pull blocks.

to one sample for each 100 timesteps, with each sample being the mean value of the preceding 100 timesteps. We observe immediately that the data carries oscillations on different time scales which match our general expectations for sliding involving periodic surfaces. By applying a Savgol filter to the data with a polynomial order of 5 and a window length of 150 data points (corresponding to a sliding distance of 3 Å or a time window of 15 ps) we can qualitatively point out at least two different frequencies of oscillation. During the first 10 Å of sliding, seen in Fig. 2.1a, we see roughly three waves on the Savgol filter corresponding to a relatively high frequency, while for the duration of 100 Å of sliding, seen in Fig. 2.1b, the same Savgol filter reveals a lower frequency on top, creating the visual pattern of a wavepacket. The data does not indicate signs of stick-slip behavior as otherwise found in other studies, e.g. by Zhu and Li [27] for graphene on gold, who saw a more typical saw tooth shape in the force trace. Besides the difference in the substrate material, using gold instead of silicon, they used a lower sliding speed of 10 m/s and a soft spring of  $K = 10 \text{ N/m}$ . By adopting these parameters we get a slightly different force trace behavior as shown in Fig. 2.1c and Fig. 2.1d. This parameter change results in a loss of symmetry in the force oscillations, but it still does not produce any significant discontinuities in the trace. By keeping the spring constant at  $K = 10 \text{ N/m}$  and lowering the sliding speed further down to 1 m/s, we achieve a more considerable stick-slip behavior as shown in Fig. 2.1e and Fig. 2.1f. Considering all three simulations, we might classify the results from the default settings,  $K = \infty, v = 20 \text{ m/s}$ , as smooth sliding,  $K = 10 \text{ N/m}, v = 10 \text{ m/s}$ , as a transition phase with possible occasional slipping, and  $K = 10 \text{ N/m}, v = 1 \text{ m/s}$  as a more typical stick-slip behaviour. This confirms the qualitative observation that stick-slip behavior is suppressed with stiff springs [29] and high sliding speed [26]. Having a low sliding speed comes with a high computational cost which is the reason that we choose a relatively high sliding speed of 20 m/s. The choice of an infinite spring constant is related to the stability of the measurements and is discussed later in this chapter.

(a)  $K = \infty$ ,  $v = 20 \frac{\text{m}}{\text{s}}$  (10 Å sliding).(b)  $K = \infty$ ,  $v = 20 \frac{\text{m}}{\text{s}}$  (100 Å sliding).(c)  $K = 10 \frac{\text{N}}{\text{m}}$ ,  $v = 10 \frac{\text{m}}{\text{s}}$  (10 Å sliding).(d)  $K = 10 \frac{\text{N}}{\text{m}}$ ,  $v = 10 \frac{\text{m}}{\text{s}}$  (100 Å sliding).(e)  $K = 10 \frac{\text{N}}{\text{m}}$ ,  $v = 1 \frac{\text{m}}{\text{s}}$  (10 Å sliding).(f)  $K = 10 \frac{\text{N}}{\text{m}}$ ,  $v = 1 \frac{\text{m}}{\text{s}}$  (100 Å sliding).

**Figure 2.1:** Force traces of the friction force component  $F_{\parallel}$  parallel to the sliding direction acting from the substrate on the full sheet. The force traces are plotted against the sliding distance (lower x-axis) and the corresponding sliding time (upper x-axis). The sliding distance is measured by the displacement of the virtual atom tethering the sheet. The red line represents a Savgol filter with polynomial order 5 and a window length of 150 data points (corresponding to a sliding distance of 3 Å or a time window of 15 ps). Each row, (a,b), (c,d), (e,f), represents a different choice of the spring constant  $K$  and sliding speed  $v$ , while the columns show the same result for two different time scales. The default settings are represented in figures (a) and (b).



By performing a Fourier Transform on the data, using the default parameters, we can quantify the leading frequencies observed in Fig. 2.1a and Fig. 2.1b. The Fourier transform is shown in Fig. 2.2a, and by plotting the two most dominant frequencies  $f_1 = 0.0074 \text{ ps}^{-1}$  and  $f_2 = 0.0079 \text{ ps}^{-1}$  as a sine sum,  $\sin(2\pi f_1) + \sin(2\pi f_2)$ , we find a qualitatively convincing fit to the observed wavepacket shape as seen in Fig. 2.2b. We convert the frequencies according to that of a wavepacket. By using the trigonometric identity

$$\begin{aligned}\sin(a+b) &= \sin(a)\cos(b) + \cos(a)\sin(b), \\ \sin(a-b) &= \sin(a)\cos(b) - \cos(a)\sin(b),\end{aligned}$$

and decomposing the frequencies as  $f_1 = a - b$ ,  $f_2 = a + b$ , we can rewrite the sine sum as the sinusoidal product

$$\begin{aligned}\sin(2\pi f_1) + \sin(2\pi f_2) &= \sin(2\pi(a-b)) + \sin(2\pi(a+b)) \\ &= \sin(2\pi a)\cos(2\pi b) - \cancel{\cos(2\pi a)\sin(2\pi b)} + \sin(2\pi a)\cos(2\pi b) + \cancel{\cos(2\pi a)\sin(2\pi b)} \\ &= 2\sin(2\pi a)\cos(2\pi b),\end{aligned}$$

with

$$\begin{aligned}a = \frac{f_1 + f_2}{2} &= 0.0763 \pm 0.0005 \text{ ps}^{-1}, & b = \frac{f_2 - f_1}{2} &= 0.0028 \pm 0.0005 \text{ ps}^{-1}, \\ &= 0.382 \pm 0.003 \text{ \AA}^{-1}, & &= 0.014 \pm 0.003 \text{ \AA}^{-1}.\end{aligned}$$

In the latter transition, we have denoted the frequency with respect to the sliding distance by considering the default sliding speed of  $20 \text{ m/s} = 0.2 \text{ \AA/ps}$ . This makes us recognize the high oscillation frequency as  $a$  and the low frequency as  $b$ . The faster one has a period of  $T_a = 2.62 \pm 0.02 \text{ \AA}^2$  which corresponds well with the magnitude of the lattice spacing as expected theoretically, and especially that of graphene with a lattice constant of  $2.46 \text{ \AA}$ . The longer period  $T_b = 71 \pm 15 \text{ \AA}$  is not obviously explained. We notice a similarly long period oscillation for all three cases Fig. 2.1b, Fig. 2.1d and Fig. 2.1f, and thus we have no reason to believe that this is dependent on the stick-slip behavior. The initial build-up in friction force is reminiscent of friction strengthening, which is often reported [24, 30], but the periodicity goes against this idea. Instead, we might attribute it to a phonon resonance effect which might be further affected by the fact that we use periodic boundary conditions for a finite substrate.

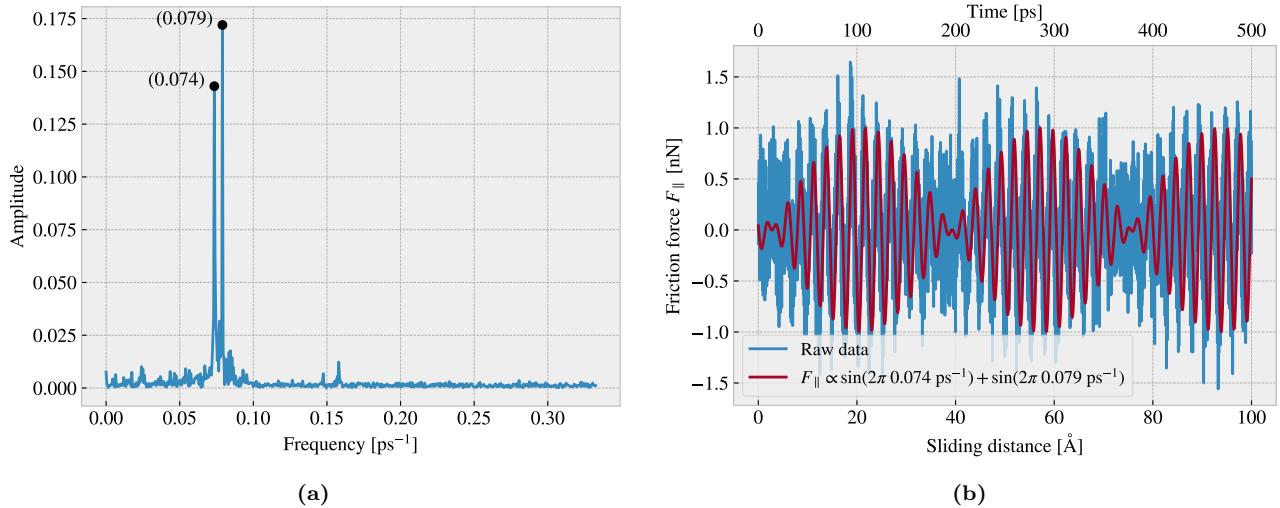


**Figure 2.2:** Fourier transform analysis of the default parameter force traces shown in Fig. 2.1a and Fig. 2.1b, but with the use of the full data length corresponding to 400 Å of sliding. (a) The Fourier transform results showing the two most dominant frequency peaks for a reduced frequency range. We excluded higher frequencies from the plot since no significant peaks were found there. (b) A comparison between the wavefunction corresponding to the two frequency peaks found in panel (a) and the raw data force trace from Fig. 2.1b.

<sup>2</sup>The uncertainty  $\Delta y$  is calculated as  $\Delta y = \left| \frac{\partial y}{\partial x} \Delta x \right|$  for uncertainty  $\Delta x$  and  $y(x)$ .

### 2.2.2 Decompositions

In the previous analysis, we considered the friction force acting on the entire sheet, including the rigid pull blocks, and with respect to the sliding direction. We found this way of measuring the friction force to be the most intuitive and reliable, but we will present the underlying arguments for this choice in the following.

Since we are only applying cuts to the inner sheet, and not the pull blocks, it might appear more natural to only consider friction on the inner sheet. If the desired frictional properties can be achieved by altering the inner sheet one can argue that any opposing effects from the pull blocks can be mitigated by simply adjusting the size ratio between the inner sheet and the pull blocks. However, when looking at the force traces decomposed with respect to the inner sheet and pull block regions respectively in Fig. 2.3a, we observe that the friction force arising from those parts is seemingly antisymmetric. That is, the frictional force exerted by the substrate on the sheet oscillates between the inner sheet and the pull blocks. Keeping in mind that normal force is only applied to the pull blocks we might take this as an intrinsic feature of the system that does not necessarily disappear with a scaling of the size ratio. Any interesting friction properties might depend on this internal distribution of forces. Hence, we hedge our bets and use the full sheet friction force as a holistic approach to avoid excluding relevant features in the measurement data.

Similarly, we might question the decision of only considering the frictional force projected onto the sliding direction as we are then neglecting the “side shift” induced during sliding. In Fig. 2.3b we show the decomposition in terms of the force components parallel  $F_{\parallel}$  and perpendicular  $F_{\perp}$  to the sliding direction respectively. We notice that the most dominant trend appears for the parallel component. One way to include the perpendicular component is to evaluate friction as the length of the force vector instead. However, this would remove the sign of the force direction and shift the mean friction force up as we see both negative and positive contributions in the parallel force trace. One option to accommodate this issue is by using the vector length for the magnitude but keeping the sign from the parallel component. However, we omit such compromises as this might make the measurement interpretation unnessecary complex, and we use only the parallel component going forward.

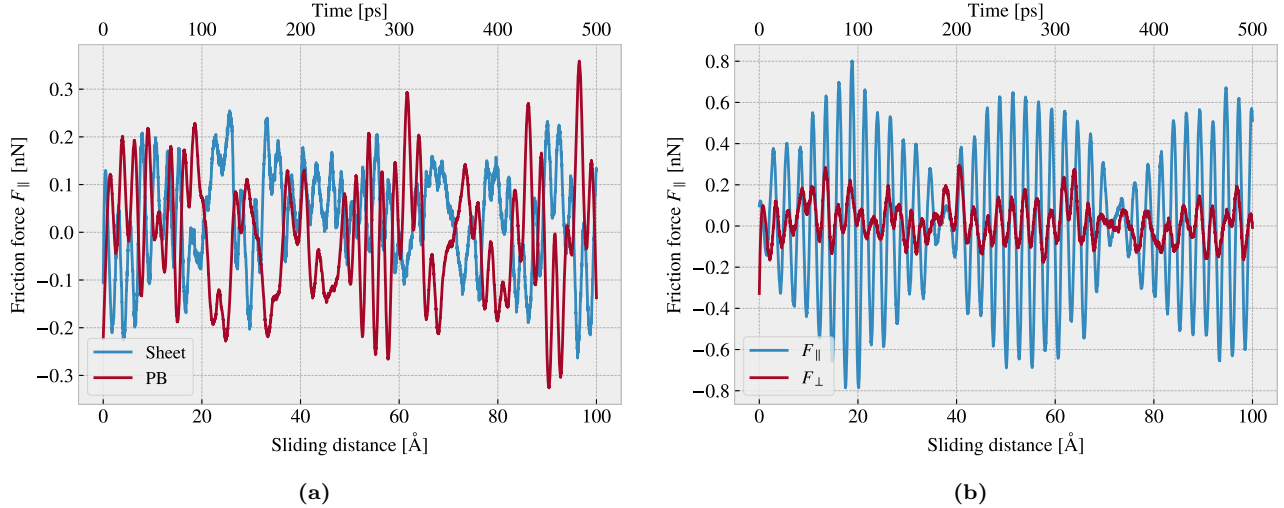


**Figure 2.3:** Friction force decomposition for the default parameter force trace shown in Fig. 2.1b. We show only the Savgol filters here. (a) Decomposition into the sheet regions inner sheet (sheet) and pull blocks (PB). (b) Decomposition into friction force parallel ( $F_{\parallel}$ ) and perpendicular ( $F_{\perp}$ ) to the sliding direction.

### 2.2.3 Center of mass path

From the previous observations of the force traces in Fig. 2.1 we found both smooth sliding and stick-slip behavior depending on the sliding speed and spring constant. Considering the force decomposition in Fig. 2.3b we know that a frictional force in the perpendicular direction to sliding is also present. By looking at the  $x, y$ -position for the sheet Center of Mass (CM) we find a qualitatively different behavior when reconsidering the spring constants and sliding speeds investigated in Fig. 2.1. These results are shown in Fig. 2.4. The default case in Fig. 2.4a shows a rather straight path with only a small side motion in comparison to the cases in Fig. 2.4b and Fig. 2.4c.

However, the CM accelerates and deaccelerates with a high frequency, much too high to be associated with the lattice spacing on the order of  $2.46 \text{ \AA}$ . One possible explanation is that the sheet and substrate constitute an incommensurate contact for which traveling kink excitations make the atoms move in such a way that the sheet CM is incremented in small “bursts”. When looking at the  $K = 10 \frac{\text{N}}{\text{m}}$ ,  $v = 10 \frac{\text{m}}{\text{s}}$  case in Fig. 2.4b we see a completely different CM path where the rapid movements align visually better with the force oscillations shown earlier in Fig. 2.1d. The CM accelerates forward and then deaccelerates in combination with a side motion that leads to the CM path making a loop as it slows down. Finally we have the  $K = 10 \frac{\text{N}}{\text{m}}$ ,  $v = 1 \frac{\text{m}}{\text{s}}$  in Fig. 2.4c which is confirmed to have stick-slip behavior from Fig. 2.1f. Here the CM path shows a more chaotic movement between accelerations, but with the rapid parts aligning visually well with the timing of the slips seen in Fig. 2.1f. We might associate the chaotic motion with thermal contributions as these are thought to be dominant at lower sliding speeds.

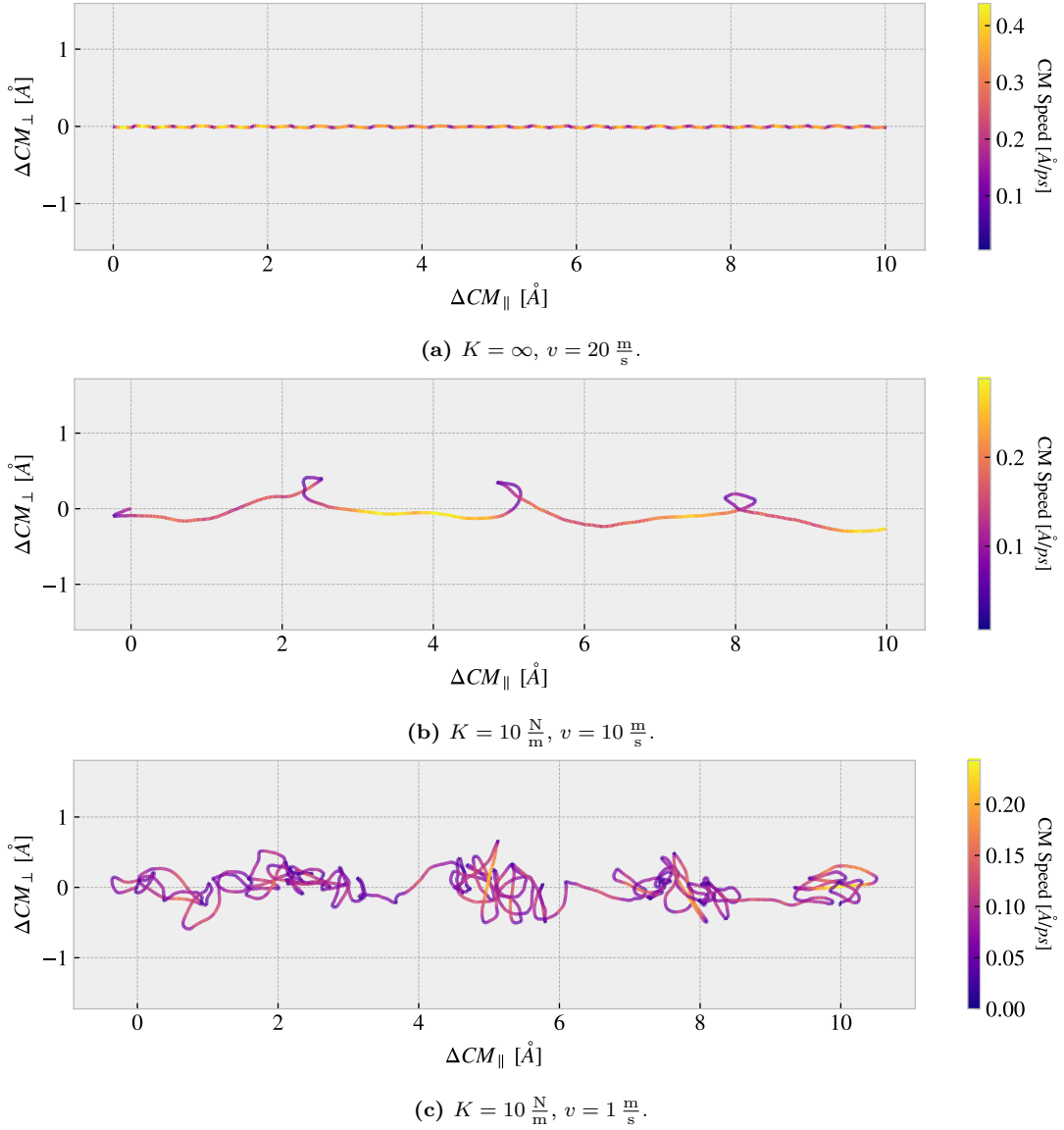


**Figure 2.4:** Sheet Center of Mass (CM) position relative to the start of the sliding phase in terms of the axis parallel to the sliding direction  $\Delta COM_{||}$  and the axis perpendicular to the sliding direction  $\Delta COM_{\perp}$ . The colors denote the absolute speed of the CM motion. Panel (a) to (c) shows different parameters used for the spring constant  $K$  and sliding speed  $v$  similar to that used in Fig. 2.1. (a) Default:  $K = \infty$ ,  $v = 20 \frac{\text{m}}{\text{s}}$ . (b) Values adopted from Zhu and Li [27]:  $K = 10 \frac{\text{N}}{\text{m}}$ ,  $v = 10 \frac{\text{m}}{\text{s}}$ . (c)  $K = 10 \frac{\text{N}}{\text{m}}$ ,  $v = 1 \frac{\text{m}}{\text{s}}$ .

## 2.3 Defining metrics for friction

In order to evaluate the frictional properties of the sheet we aim to reduce the force trace results, addressed in Sec. 2.2, into single metrics describing the kinetic and static friction respectively.

### 2.3.1 Kinetic friction

We measure kinetic friction as the mean of the friction force trace. More precisely, we take the mean value of the last half of the dataset in order to ensure that we are sampling from a stable system. For a full sliding simulation of 400 Å our mean value will be founded on the last 200 Å (1000 ps) of sliding. In Fig. 2.5a we have shown the force trace for the first 10 Å of sliding together with a 50% running mean window. The choice of such a short sliding distance is merely to illustrate the sampling procedure, and we see that the final mean estimate (marked with a dot) takes a negative value due to the specific cut-off of the few oscillations captured here. Nonetheless, one approach to quantifying the uncertainty of the final mean estimate is to consider the variation of the running mean preceding the final mean value. The more the running mean fluctuates the more uncertainty associated with the final estimate. Only the running mean “close” to the ending should be considered, since the first part will rely on data from the beginning of the simulation. From the Fourier analysis in Sec. 2.2.1 we found the longest significant oscillation period to be  $\sim 71$  Å. Hence, we find it reasonable to use the standard deviation (std) for the last  $\sim 71$  Å of the running mean window to evaluate the fluctuations. When including the full sliding length this corresponds to the last  $\sim 35\%$  of the running mean window ( $400 \text{ Å} \cdot 50\% \cdot 35\% \approx 71 \text{ Å}$ ). We consider the std as an estimate of the absolute error and calculate the relative error by a division of the final mean value. In Fig. 2.5b we showcase a running relative error based on the std, with a window of length 35% of the mean window, in a continuation of the illustrative case from Fig. 2.5a. In this case, we get an extremely high relative error of  $\sim 257\%$ , but this is consistent with the fact that the short sampling period leads to an unphysical negative value which should be associated with high uncertainty.

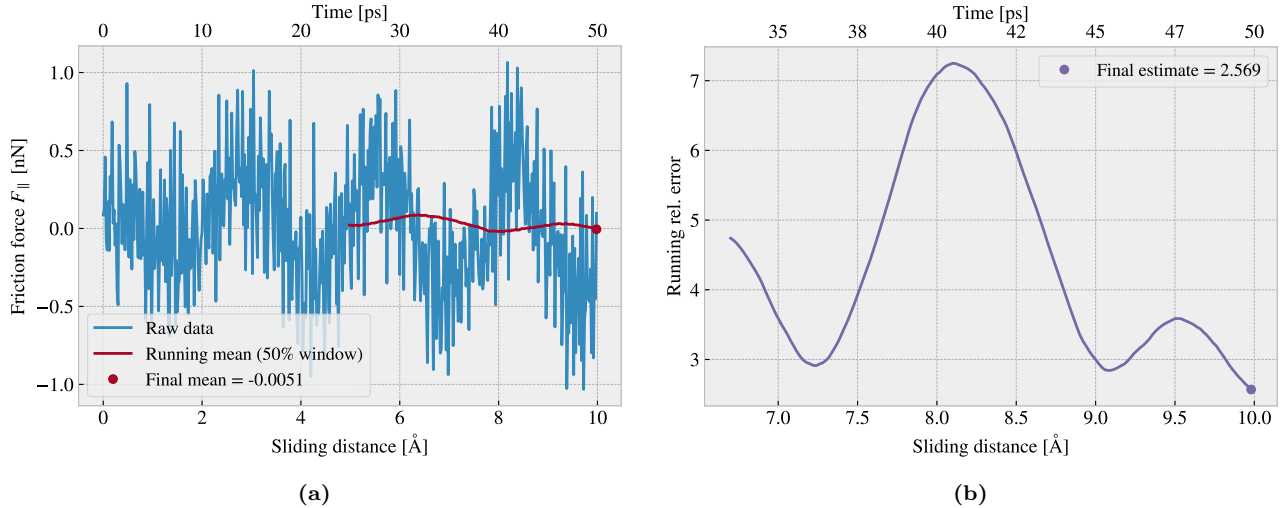


**Figure 2.5:** Supporting figures for the description of the kinetic friction metric and corresponding uncertainty for an example using a reduced sliding distance of 10 Å. (a) The running mean for the force trace with a window length of 50% of the sliding length in this example. (b) The running relative error calculated using the standard deviation for the 35% running window of the running mean (red line in panel (a)). For both figures, the running value is displayed at the end of their respective corresponding windows.

When including the full dataset of 400 Å of sliding, such that the std window actually matches with the longest period of oscillations expected, we get a final relative error of  $\sim 12\%$  as shown in fig Fig. 2.6. This is arguable just at the limit of an acceptable error, but as we shall see later on in Sec. 2.6 this high relative error is mainly associated with the cases of low friction. When investigating different configurations under variation of load and strain we see a considerably lower relative error as the mean friction evaluates to higher values. One interpretation of this finding is that the oscillations in the running mean are not substantially influenced by the

magnitude of the friction. In that case, the relative error will spike for the low friction cases, and the absolute error might be the more reliable measure, i.e. using simply the std without dividing by the final mean value.

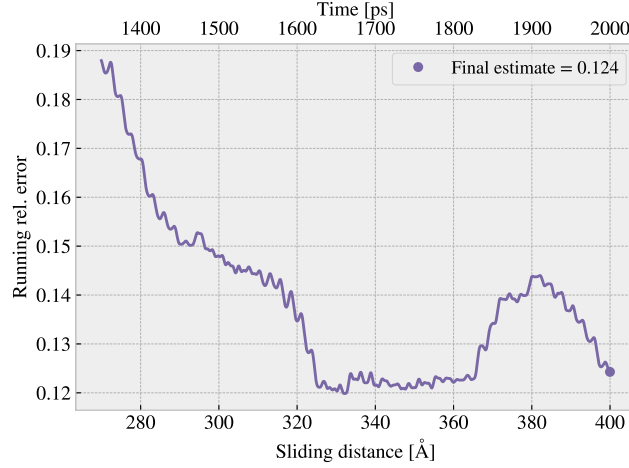


**Figure 2.6:** Running relative error calculated from the standard deviation (std) for a full 400 Å sliding simulation. The running std window is 70 Å (35% of the running mean window, which is 50% of the full sliding length).

### 2.3.2 Static friction

The maximum value is one of the common choices for addressing static friction, even though the definition of static friction is a bit vague. When considering the force traces in Fig. 2.1 we observe that the force oscillations increase in magnitude toward a global peak at  $\sim 20$  Å. Thus, one could be inclined to identify this peak as the maximum value associated with the static friction force. However, as we have already clarified, this steady increase in friction is part of a slower oscillation that repeats with a period of  $\sim 71$  Å. By plotting the top three maximum values recorded during a full 400 Å simulation, for 30 logarithmically spaced load values in the range  $[0.1, 100]$  nN, we observe that the global maximum rarely falls within this first oscillation period as shown in Fig. 2.7a. Only 2 out of 30 global maxima and 4 out of 90 top three maxima can be associated with the start of the sliding by this definition. Thus, this result suggests that our default system does not yield a static friction response in the sense of an initial increase in friction due to a depinning of the sheet from the static state. Several modifications to the system parameters may enhance the likelihood of observing a substantial static friction response. These include prolonging the initial relaxation time, as static friction is believed to increase logarithmically with time [31], or increasing the sliding force more slowly by decreasing the sliding speed or utilizing a soft spring tethering. As an attempt to test the latter part of this hypothesis, we conducted a series of simulations with different spring constants,  $K \in [5, 200]$  nN, including also  $K = \infty$ , while maintaining the relaxation period and sliding velocity at their default values. The results shown in 2.7b do not support this hypothesis since the reduction of the spring constant did not lead to the maximum friction peak appearing within the first oscillation period. We acknowledge that this outcome might be compromised by our choice of the relaxation period or sliding speed. However, given the ambiguity surrounding the determination of static friction, we will mainly concern ourselves with kinetic friction in the remainder of this thesis.

## 2.4 Out-of-plane buckling

The out-of-plane buckling is one of the motivations for investigating the application of Kirigami cuts in the context of friction properties. Therefore, we perform a stretch simulation, at low temperature ( $T = 5$  K) without any substrate, in order to verify that we can reproduce an out-of-plane buckling with the Tetrahedron and Honeycomb patterns. For this investigation, we consider the Tetrahedron (7, 5, 1) and the Honeycomb (2, 2, 1, 5) pattern in comparison to the non-cut sheet. We quantify the out-of-plane buckling by assessing the distribution of atoms along the z-direction (perpendicular to the plane) during straining. We calculate the minimum and maximum z-value as well as the atom count quartiles 1%, 10%, 25%, 50% (median), 75%, 90% and 99% as shown

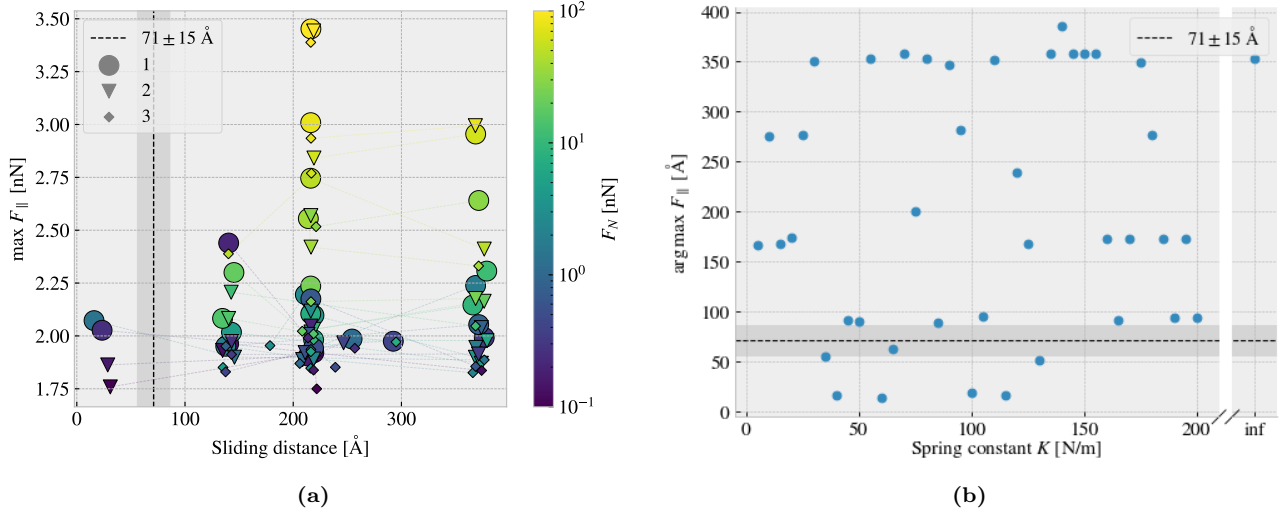


**Figure 2.7:** Investigation of the sliding displacement corresponding to the maximum friction force peaks. The dotted line, along with the gray-shaded area indicating the degree of uncertainty, represents the slowest significant oscillation period identified in the data from the Fourier analysis in Fig. 2.2a. This line serves as a threshold for determining whether a peak falls within the initial portion of the sliding simulation. (a) The top three maxima for simulations with varying loads; 30 logarithmically spaced loads in the range  $[0.1, 100]$  nN. The marker shapes denote the top 1, 2 and 3 respectively and the color denotes the normal load. (b) The sliding displacement corresponding to the friction maxima for simulations with varying spring constant; 40 uniformly spaced values in the range  $K \in [5, 200]$  N/m in addition to  $K = \infty$ .

in Fig. 2.8. The Tetrahedron and Honeycomb patterns show significant buckling in comparison to the non-cut sheet, which only exhibits minor buckling of  $\sim 2$  Å, which is of the same order as the lattice spacing. We notice that the Tetrahedron pattern buckles more in consideration of the minimum and maximum peaks while the remaining quantiles seem to be more closely spaced than for the Honeycomb. By addressing the simulation results visually, using the *Open Visualization Tool OVITO*, we find that this can be attributed to fringes on the edge “flapping around” and thus increasing the minimum and maximum values. This is also evident from the simulation with the substrate seen in ?? in ??.

Given the confirmation of out-of-plane buckling in a vacuum, as seen in Fig. 2.8, we reintroduce the substrate in order to investigate whether this effect carries over to a changing contact area. For this simulation, we raise the temperature to the default value of  $T = 300$  K. We keep the normal force off and let the sheet stick purely by the adhesion forces between the sheet and substrate. We quantify the contact area through the relative number of atoms in the sheet within chemical range of the substrate. The cut-off for this interaction is set to 4 Å, adopted from [24], corresponding to  $\sim 120\%$  the LJ equilibrium distance. Usually, the contact area is calculated as the number of contacting atoms multiplied by an associated area for each atom. However, since we are not interested in the absolute value of the area, but rather the relative change, we omit the multiplication factor. That is, we consider the relative number of atoms within the contact range as our metric of choice, which is proportional to the contact area. The relative contact for the three configurations No cut, Tetrahedron (7, 5, 1) and Honeycomb (2, 2, 1, 5) during straining are shown in Fig. 2.9. The figure reveals a significant drop in relative contact as the sheets are strained, which agrees qualitatively with the buckling observed in Fig. 2.8 without the substrate. The Honeycomb pattern turned out to be both the most stretchable, with a rupture strain of 1.27, and the one with the biggest decrease in relative contact with a minimum of approximately 43%. Notice, that the relative contact is never actual 1.0 but instead reaches a maximum of 96% at zero strain. This is attributed to the temperature fluctuations and the choice of cut-off.

Selected frames from the simulation result are shown in ?? which reveals a bit more information on how the buckling occurs. The Tetrahedron pattern deforms rather quickly and smoothly into small tetrahedron spikes, as the name suggests. In the Honeycomb pattern, on the other hand, the deformations initiate from one side first. As the sheet stretches, more rows of the pattern are activated, producing the honeycomb-looking shape when seen from above. Both patterns exhibit a small increase in relative contact when they are approaching

their rupture strain, which agrees with the results from Fig. 2.8 where the buckling reduces slightly towards the rupture strain.

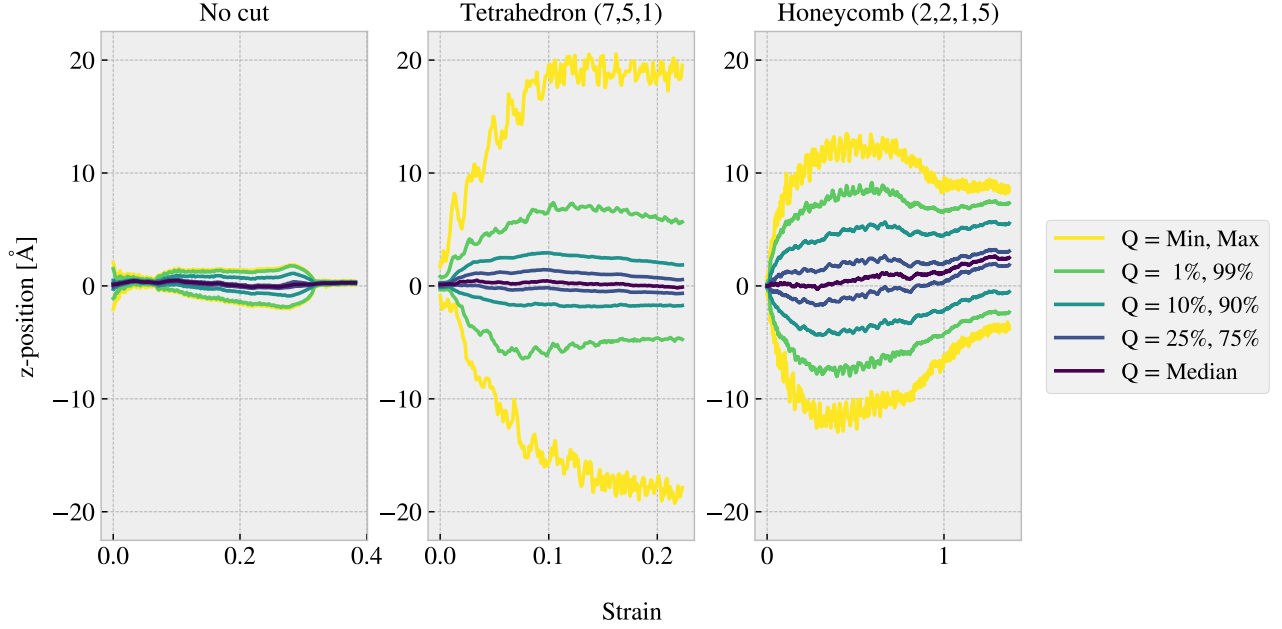


**Figure 2.8:** The out-of-plane buckling during straining for the non-cut (No cut), Tetrahedron (7, 5, 1), and Honeycomb (2, 2, 1, 5) pattern respectively in vacuum at low temperature  $T = 5$  K. The buckling is quantified by the distribution of the atom z-positions, which are perpendicular to the sheet plane, and the colors indicate selected quantiles. The rupture strain for each pattern, from left to right, is 0.38, 0.22, and 1.37, respectively. The results indicate that the Tetrahedron and Honeycomb patterns exhibit significant out-of-plane buckling in comparison to the non-cut sheet.

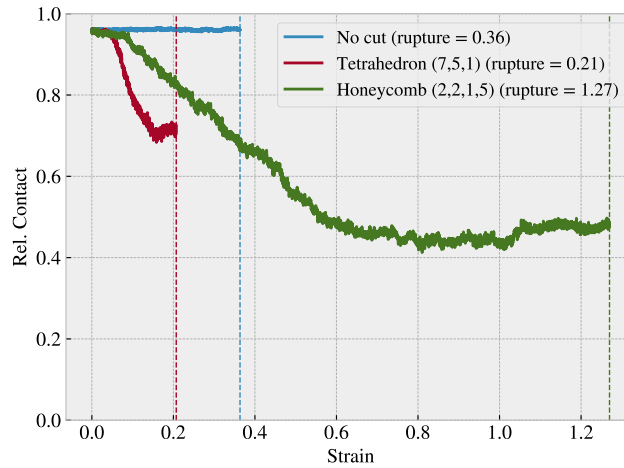


**Figure 2.9:** The relative contact during straining of the non-cut (No cut), Tetrahedron (7, 5, 1), and Honeycomb (2, 2, 1, 5) pattern respectively in contact with a substrate. The relative contact is given as the relative number of atoms in the sheet within chemical interaction range. The cut-off for the interaction range is  $4 \text{ \AA}$  corresponding to  $\sim 120\%$  the LJ equilibrium distance. No normal force is applied and the temperature is kept at  $T = 300$  K.



## 2.5 Investigating default parameters

We carry out a more extensive investigation of the friction dependence on temperature  $T$ , sliding speed  $v$ , spring constant  $K$ , and timestep  $dt$ . This is done partly to understand how the dependencies relate to the theoretical, numerical and experimental results, and partly to understand how these parameters affect the stability of our system. We use the default parameters presented in Table 2.1 and investigate the results as we change parameters, one at a time. We keep the load at 1 nN. We consider the mean friction force parallel to the sliding direction for the full sheet, sampled from the last half of the simulation as described in Sec. 2.3, representing the kinetic friction. The results are shown in Fig. 2.10, where the shaded area (connected linearly) denotes the absolute error defined by the std as described in Sec. 2.3 as well.

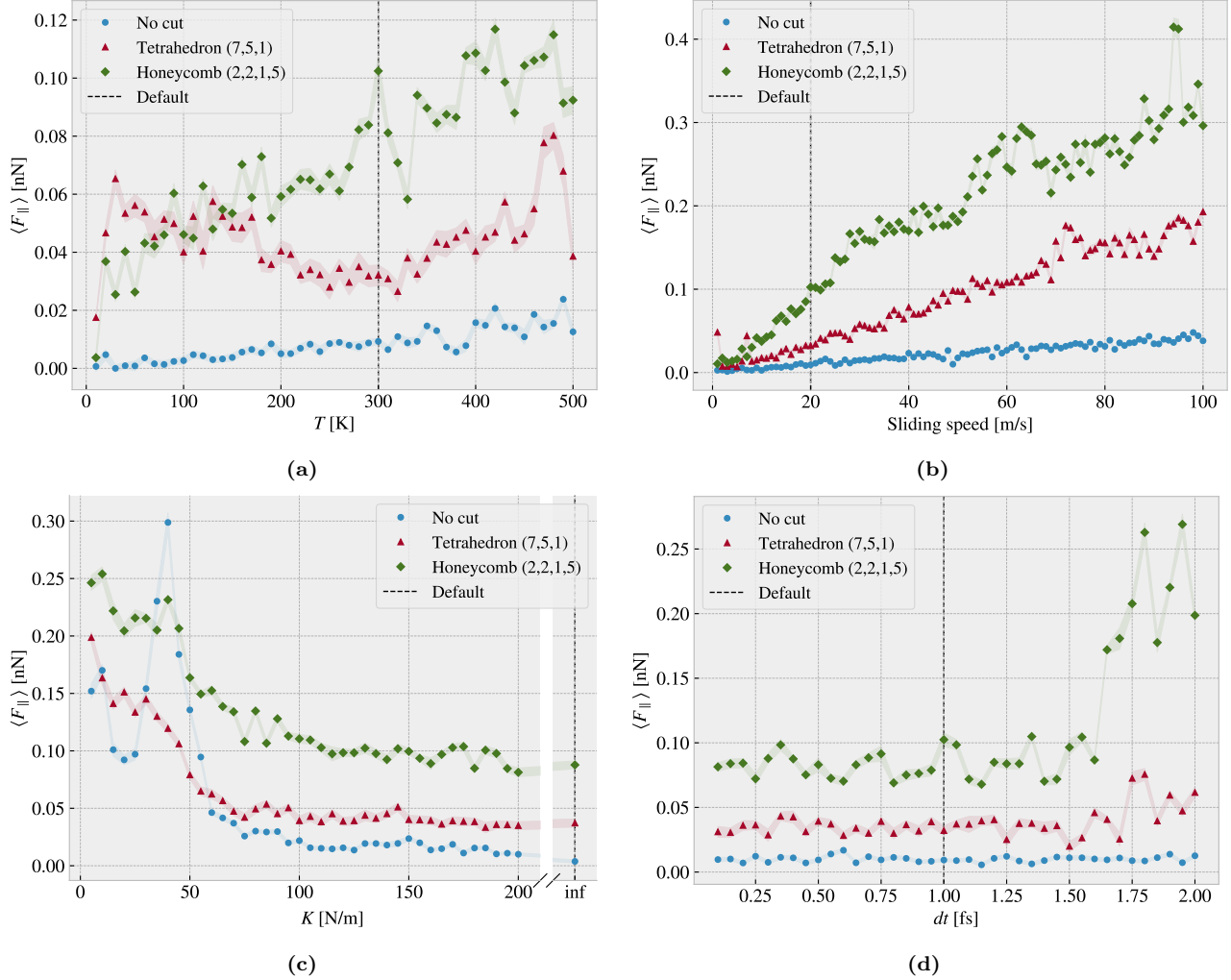


**Figure 2.10:** Investigation of the friction dependencies to the selected parameters: Temperature  $T$  (a) sliding speed (b), spring constant  $K$  (c) and timestep  $dt$  (d), for the non-cut sheet, the Tetrahedron (7, 5, 1), and the Honeycomb (2, 2, 1, 5) patterns. The dotted line denotes the default parameter choice and the shaded area denotes the estimated absolute error.

From the temperature investigation in Fig. 2.10a we find an overall increasing kinetic friction with temperature for both the non-cut sheet and the Honeycomb pattern. The Tetrahedron pattern shows both decreasing and increasing trends. The general trend shows a convex curve in the range (30–480 K) with a minimum around our default choice of 300 K, but with rapid fluctuations at the start (10–30 K) and end region (480–500 K). Similar fluctuations are also seen for the Honeycomb pattern, although it shows an underlying increasing trend throughout. When comparing the non-cut sheet and the Honeycomb pattern we observe that the slope for the increasing trend is higher for the Honeycomb pattern. From the predictions of the Prandtl–Tomlinson model and



experimental results we expect to find a decrease in friction with increasing temperature which disagrees with our results. However, in similar MD-based studies by Guerra et al. [32] they report that the friction dependence on temperature reverses at high sliding speed. They attribute this to the crossover from the diffusive to the ballistic regime taking place at a sliding speed of 1 to 10 m/s. This agrees with our observations since we are using a sliding speed of 20 m/s. The increase in friction with temperature also agrees with the predictions from the 2D Frenkel-Kontorova model [33]. In the absence of any clear suggestions from the results regarding an appropriate temperature, we take the common choice of using the room temperature 300 K. The non-cut and Tetrahedron friction shows to be rather stable around this temperature choice, although we do see some significant fluctuations for the Honeycomb pattern in this range. However, we do not regard this as a critical feature.

From the sliding speed investigation in Fig. 2.10b we generally find increasing friction with sliding speed. Due to the relatively high sliding speed used in these simulations, we expect a viscous friction  $F_{\text{fric}} \propto v$  as reported by Guerra et al. [32] and predicted by the Prandtl-Tomlinson model. In general, this aligns rather well with our results, especially for the non-cut sheet. However, the Tetrahedron and Honeycomb sheets seem to fall slightly into a sublinear relationship as it approaches higher sliding speeds. This behavior could potentially be attributed to velocity saturation, a phenomenon predicted by the Prandtl-Tomlinson model without considering the damping effect of the thermostat. On the other hand, experimental results generally show a logarithmic increase in friction with sliding speed, which may align better with the behavior observed for the Tetrahedron pattern. Furthermore, we find that the Tetrahedron and Honeycomb patterns both display indications of local fluctuations that could be attributed to phonon resonance effects, as discussed in relation to the Frenkel-Kontorova models. Our choice of a sliding speed at 20 m/s mainly reflects a consideration of computational cost, but the fact that no immediate resonance fluctuations appear in the proximity of this value supports the choice further.

From the investigation of the spring constant parameter in Fig. 2.10c, we observe a significant decrease in friction with increasing spring constant. This can be attributed to the transition from a stick-slip influenced regime to a smooth sliding regime as evidenced by the force traces in Fig. 2.1. For soft springs (low  $K$ ) the friction response is quite sensitive to the specific choice of spring constant which is especially seen for the non-cut sheet around  $K = 40$  N/m. Thus, in order to avoid this domain we settled for the infinitely stiff spring ( $K = \infty$ ). This is also considered a more favorable option due to its ability to provide greater standardization of the simulations since it allows for a more controlled movement of the sheet.

Finally, we consider the numerical stability of the simulation result as we vary the simulation timestep in Fig. 2.10d. The results indicate that the simulation is generally stable below a timestep of  $\sim 1.5$  fs, beyond which instability arises for the cut sheets (Tetrahedron and Honeycomb). This confirms that our choice of timestep is reasonable, but we do observe some fluctuations that are more pronounced for the cut sheets. These fluctuations imply that randomness plays a role in our simulations and that the cut sheets exhibit relatively higher instability compared to the non-cut sheet. Further investigation through varying the random seed for the initial velocity and thermostat could shed more light on this matter. In the meantime, we may consider these fluctuations as a sign that the uncertainty in our results is higher than our estimation from using the running mean and running std. For the Honeycomb sheet, these fluctuations are on the order of  $\pm 0.017$  nN. This also aligns with the observation that the friction values obtained for the default parameters are not exactly equal across all simulation results in Fig. 2.10. We find the estimated error by the fluctuations with timestep to match these deviations rather well.

### 2.5.1 Computational cost

Our simulations are carried out on a CPU cluster made available by the University of Oslo. This allows us to run multiple simulations at once and with each simulation running in parallel on multiple CPU cores as well. When selecting the simulation parameters, we also need to keep in mind the computational cost. Given that the chosen parameters will be applied to multiple simulations, any increase in computational time will be multiplied by the number of intended simulations, which is roughly 10,000. The computational cost is especially dependent on the timestep and the sliding speed as this will affect the number of computations needed for a full simulation. As an extension of the investigation from Fig. 2.10 we report on the computational times associated with temperature, sliding speed, spring constant and timestep. By retrieving the computational time used for the parameter investigation in Fig. 2.10 we get the timings shown in Fig. 2.11. Note that these timings are only based on a single simulation for each parameter as opposed to an average over multiple runs which is necessary for more reliable data.

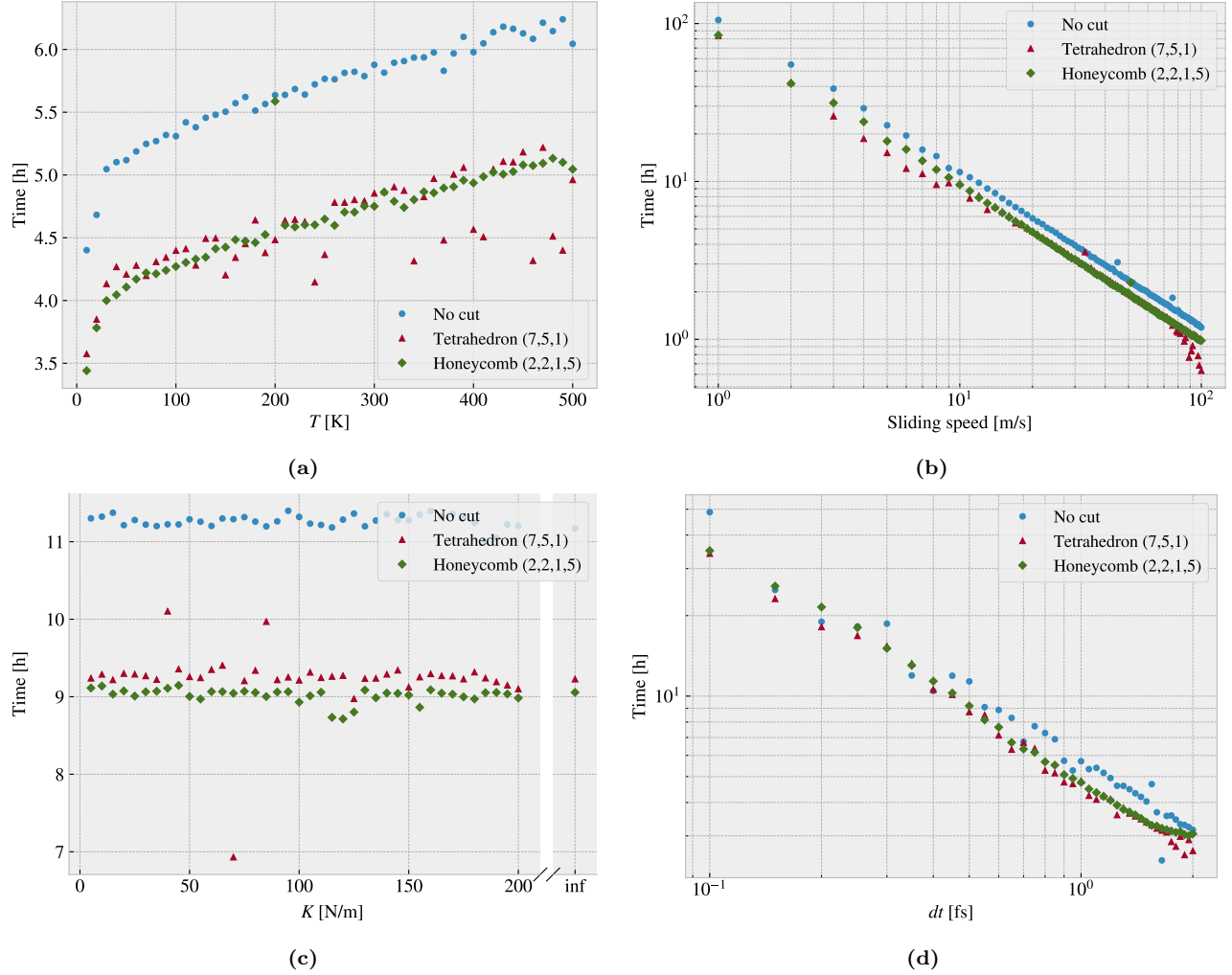


**Figure 2.11:** The computational timings for the simulations carried out for the parameter investigation in Fig. 2.10 in terms of CPU hours running on 16 cores on the CPU cluster. The timing  $t$  with respect to the sliding speed  $v$  is found to follow  $t \propto v^{-0.977 \pm 0.005}$  while the timing for the timestep length  $dt$  follows  $t \propto dt^{-0.87 \pm 0.02}$ .

The computational time is governed by the number of timesteps in the simulation and the time used per simulation timestep. For a fixed sliding distance, the number of timesteps in the simulation is inversely proportional to sliding speed and similar inversely proportional to timestep  $dt$ . From the results in Fig. 2.11 we find that the sliding speed obeys this expectation rather well by  $t \propto v^{-0.977 \pm 0.005}$ . The timing did not increase as strongly as expected with timestep length, falling above the  $1/dt$  relation with  $t \propto dt^{-0.87 \pm 0.02}$ . Moreover, we find that increasing temperature also makes for an increased computation time. This can be attributed to an increase in the computation time associated with the force calculations. The rising temperature is associated with more fluctuations in the system which might yield more atoms within the force calculation cutoffs for each computation. This kind of consideration can also be attributed to the reason for the deviating timing relationship with  $dt$ . Finally, for the spring constant, we did not see any noticeable effect on timing.

In general, we have selected our simulation parameters: temperature, sliding speed, spring constant, and timestep, based on numerical stability and computational cost. For the timestep, we found that a value of 1 fs, commonly used in similar studies [26, 27], produced stable results while higher values were prone to instabilities and lower values were computationally expensive. The sliding speed was chosen primarily based on computational cost, with a default value of 20 m/s being a reasonable compromise between computational efficiency and relatability to the lower values more commonly used in other studies. Although a lower sliding speed could lead to an interesting regime governed by stick-slip motion, it represents a factor of 20 increase in computational time. Since stick-slip motion is out of reach based on the chosen sliding speed, we found that

using an infinitely stiff spring  $K = \infty$  was the most reasonable option to ensure stable results. Finally, the temperature investigation did not provide much guidance for a specific choice, so we settled for the standard choice of room temperature  $T = 300$  K.

## 2.6 Strain and load dependencies

So far, we have carried out a general analysis of the system behavior under the influence of various simulation parameters. This lays the foundation for the remaining study as we now shift our intention towards friction dependence on strain and load.

### 2.6.1 Pressure reference for normal load

We consider a load range of 0.1–10 nN which coincides with the general range investigated in other MD studies [24, 27]. In order to relate the magnitude of this load we provide a short calculation of the corresponding pressure. We will use the pressure underneath a stiletto-heeled shoe as a high-pressure reference from a macroscale perspective. The diameter of a stiletto-heeled shoe can be less than 1 cm [34], and hence an 80 kg man<sup>3</sup> standing on one stiletto heel, with all the weight on the heel, will generate a pressure

$$P = \frac{F}{A} = \frac{mg}{r^2\pi} = \frac{80 \text{ kg} \cdot 9.8 \frac{\text{m}}{\text{s}^2}}{\left(\frac{10^{-2} \text{ m}}{2}\right)^2 \pi} = 9.98 \text{ MPa}.$$

The fact that the pressure under a stiletto heel can get this high, actually greater than the pressure under an elephant foot, is an interesting realization in itself that is often used in introductory physics courses [35]. Nonetheless, this serves as a reasonable upper bound for human executed pressure. With a full sheet area of  $\sim 212 \text{ nm}^2$  our load range of 0.1–10 nN corresponds to a pressure of 0.47–47 MPa which relates reasonably to our macroscale reference. This pressure might be incompatible with various industrial purposes, but with no specific application in mind, this serves as a decent reference point. Notice, that if we consider a human foot with the area  $113 \text{ cm}^2$  [36] the pressure drops to a mere 70 kPa corresponding to only  $\sim 0.01$  nN.

### 2.6.2 Strain dependency

We consider the effects of stretching the sheet using the non-cut, Tetrahedron (7, 5, 1) and Honeycomb (2, 2, 1, 5) sheet as used so far. While we consider the actions of “stretching” and “straining” to be synonyms we will describe the sheet deformation state with the technical term *strain*. The strain describes the change in length relative to a reference length. We use the relaxed sheet as our reference length  $L_0$  for which the straining towards a larger length  $L$  corresponds to the strain  $\epsilon = (L - L_0)/L_0$ . Thus a strain of 0 corresponds to the relaxed sheet and a strain of 1 corresponds to a doubling of sheet length. Notice that the measure of strain is dimension specific, but we will only consider the y-direction which corresponds to the direction of applied strain in the simulations. For each configuration, we run a rupture test where the given sheet is stretched under zero load, but still under the influence of adhesion from the substrate. The rupture strain is then recorded, and multiple new simulations are initiated with strain values uniformly spaced between zero and the rupture strain. For the load we use 0.1, 1 and 10 nN. First, we aim to reproduce the contact investigation from Fig. 2.9. We quantify the relative contact as described in Sec. 2.4, but we convert this into a single metric for a given simulation by considering the mean of the last 50% of the data points, similar to what we have done for the mean friction. We also adopt a similar method for quantifying the error (see Sec. 2.3). Fig. 2.12a shows a significant decrease in relative contact with strain for the kirigami patterns. This agrees qualitatively with the non-loaded continuous strain simulations in Fig. 2.9. This result implies that the change in contact is not governed by a momentum effect during stretching, as each simulation now keeps a constant strain throughout. From an asperity theory point of view, the reduction in contact area is theorized to induce a linearly dependent reduction in friction. However, when considering the kinetic friction in Fig. 2.12b we find that this is not the case. For the Tetrahedron and Honeycomb patterns, we find that the friction initially increases with a decreasing contact area. Yet, these are not simply inversely proportional as the friction force suddenly dips down and up again, in the strain range of 0.08–0.11 for the Tetrahedron and 0.73–1.05 for the Honeycomb pattern. When considering the non-cut sheet, we find that both the contact area and friction remain seemingly unaffected by strain. This indicates that the

---

<sup>3</sup>Yes, a man can certainly wear stiletto heels.

contact area is not a dominating mechanism for friction in our system, although the non-linear friction-strain curve might be correlated with a decrease in contact area through an underlying mechanism related to the out-of-plane buckling. This can be supported by the fact that the contact-strain and friction-strain curves for the Honeycomb pattern both show signs of a discontinuous jump around a strain of 0.32.

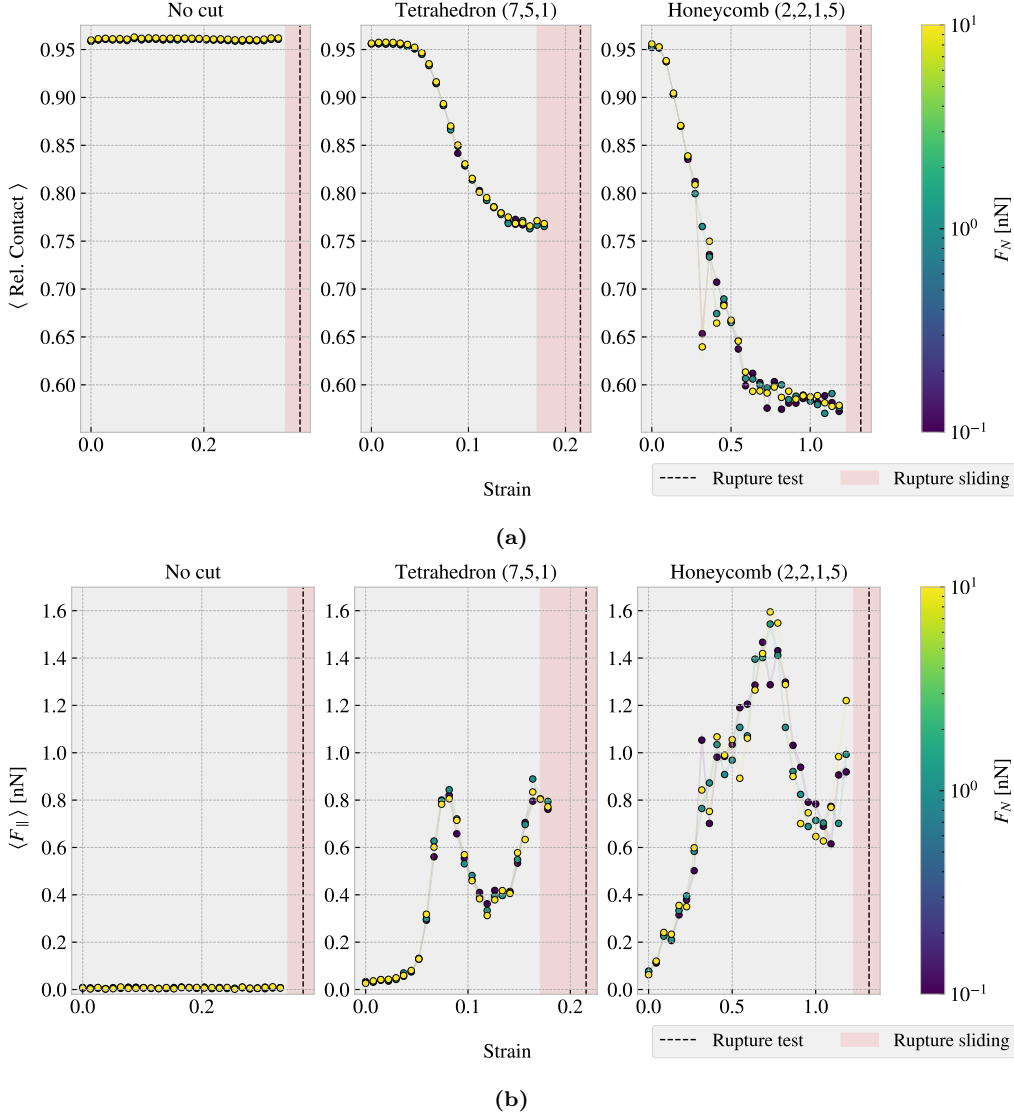


**Figure 2.12:** Investigation of the frictional behavior for the non-cut, Tetrahedron (7, 5, 1) and Honeycomb (2, 2, 1, 5) sheet under varying strain, consisting of 30 strain values uniformly spaced between 0 and the rupture strain in combination with loads 0.1, 1 and 10 nN. The shaded area, connecting the dots linearly, denotes the absolute error. The red shade denotes the strain range where ruptures occurred during loaded sliding while the black-dotted line represents the rupture point in the non-loaded rupture test. (a) The average relative contact defined as the relative number of atoms within a contact threshold of 4 Å to the substrate. The absolute error is generally on the order  $10^{-4}$ . (b) The average mean friction force. The absolute error is generally on the order  $10^{-3}$  nN.

Since the non-cut sheet exhibits a flat friction-strain profile we cannot attribute the behavior to an increased tension either. Zhang et al. [30] reported that the friction for a graphene sheet decreases with tension which qualitatively contradicts our observation for the Tetrahedon and Honeycomb patterns and supports that tension is not a governing mechanism for these observations. Instead, we might attribute the results to a commensurability effect which is predicted by the Frenkel-Kontorova models and observed in both numerical and experimental

studies. We might also point to a change in the structural stiffness which is reported as an important feature by H. J. Kim and D. E. Kim [37].

We notice that the initial friction value of the non-strained sheet varies among different configurations, with the non-cut sheet exhibiting the lowest initial friction value ( $\sim 7 \times 10^{-4}$  nN), the Tetrahedron sheet having a slightly higher value ( $\sim 0.03$  nN), and the Honeycomb sheet exhibiting the highest ( $\sim 0.07$  nN). This is more clearly shown in the parameter investigation in Fig. 2.10. This supports the idea of a commensurability effect as the removal of atoms might affect the lattice structure of the sheet slightly. However, the magnitude of this effect is generally one order of magnitude lower than the strain-induced friction effect observed for the Tetrahedron and Honeycomb patterns. We attribute this to the idea that the reorganization of the contacting atoms has significantly more impact on commensurability than removing some atoms from the lattice. We notice also that the two orders of magnitude increase in normal load did not make a significant difference in the results. The estimated absolute error marked by a shaded area in Fig. 2.12b were fairly low for both friction on the order of  $10^{-3}$  nN and relative contact on the order of  $10^{-4}$ .

By considering the increase in friction from zero strain towards the first peak of the friction-strain curve we find that the Tetrahedron pattern exhibits a relative friction increase of  $\sim 27.7$  while the Honeycomb pattern exhibits a relative increase of  $\sim 22.4$ . This is in itself an interesting result, but considering that the friction drops almost as dramatically afterward is even more unexpected. For the Tetrahedron pattern, the friction drops by  $\sim 0.51$  nN during an increased strain  $\Delta\epsilon \sim 0.04$  while for the Honeycomb pattern the friction drops  $\sim 0.98$  nN during a strain increase of  $\Delta\epsilon \sim 0.36$ . These results are promising for the aim of achieving a negative friction coefficient for a system with coupled load and strain. We will discuss this further at the end of this chapter in Sec. 2.6.4.

### 2.6.3 Load dependency

From the investigation of the strain dependency we saw that increasing the normal load from 0.1 to 10 nN did not make a considerable impact on the friction in comparison to the effect associated with strain. One special feature of our system is that we only apply load to the pull blocks, and thus we might suspect this to be of importance. Therefore, we investigate the friction under varying loads for a non-cut sheet comparing the case of loading only the pull blocks against a uniform loading of the entire sheet as shown in Fig. 2.13. Both load distributions show a seemingly non-dependent relationship between friction and load considering the size of the estimated errors. Thus, we do not find any indications that the uniform loading changes the qualitative behavior of our system.

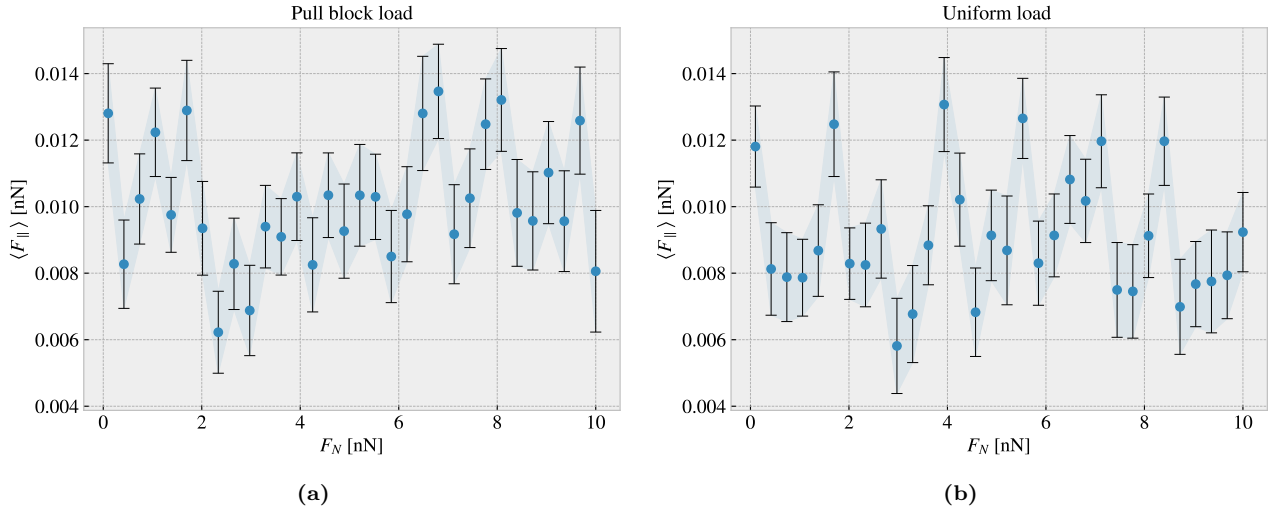


**Figure 2.13:** Multiple simulations of a non-cut sheet under various normal load values uniformly spaced in the range  $F_N \in [0.1, 10]$  nN for two different variations of loading distribution. The shading and the error bars denote the absolute error. (a) The normal loading is applied to the pull blocks only. (b) The normal loading is applied uniformly to the full sheet.

To examine the relationship between friction and normal load as the Kirigami patterns undergo strain, we conduct additional simulations with logarithmically spaced normal load values in the range of 0.1 to 100 nN. This is done for a selected subset of strain stages from Fig. 2.12, with 30 load values for each strain. We also monitor the relative contact during the increased load. The results are shown in Fig. 2.14. From Fig. 2.14b we observe that the three orders of magnitude load increase yields a small increase in friction for all Kirigami patterns. This effect is more pronounced in the figure for the non-cut sheet, but this is mainly because the friction axis shows a narrower range for this figure. It should be noted that due to the logarithmic scale of the load axis, any apparent linear trends in the figure are in fact sublinear. Nonetheless, as the normal load approaches 100 nN, there is some indication of an increase in friction reminiscent of a linear relationship. However, it is difficult to draw firm conclusions as the magnitude of the increase in friction is relatively small compared to the level of noise in the data.

For the investigation of contact area in Fig. 2.14a, we generally find an increasing contact area with load. By considering the full load from 0.1 nN to 100 nN we find the largest increase in relative contact, among the various values of relative strain, to be 0.007 for the non-cut, 0.014 for the Tetrahedron and 0.025 for the Honeycomb sheet. This constitutes a rather small change and thus it is difficult to assess how this relates to a dependency between the contact area and the friction. However, we do see that the Tetrahedron and Honeycomb patterns exhibit a larger change in contact area which aligns with the idea that the out-of-plane buckling makes them behave more like an asperity system. When plotting the friction against relative contact in Fig. 2.14c we do not find any significant evidence for a linear relationship between contact area and friction as otherwise proposed by asperity theory. Instead, from the Tetrahedron and Honeycomb pattern, we confirm that the strain-induced effects are dominant in comparison to any effects from the contact area. By studying an even larger load range we might get more insight into this relationship. Note that we have omitted the error bars in Fig. 2.14 for visual purposes, but the absolute errors for both the relative contact and friction force are on the same order of magnitude as shown in both Fig. 2.12 and Fig. 2.13.

From the friction measurements in Fig. 2.14b we find that the non-cut sheet generally produces a friction force in the range 0.005–0.0025 nN throughout the 0.1–100 nN load range. Using a ratio based friction coefficient definition ??,  $\mu_1 = F_{\text{fric}}/F_N$ , this would lead to a coefficient roughly in the range

$$\mu_1, \text{ ??}: \quad \text{No cut} \sim [10^{-4}, 0.13], \quad \text{Tetrahedron} \sim [4 \times 10^{-4}, 8.7], \quad \text{Honeycomb} \sim [9 \times 10^{-4}, 15.2].$$

However, these values mainly reflect the pooriness of this definition, as we find the values to diverge at small loads and decrease toward high loads due to the lacking linear relationship and an offset in the load curve corresponding to a finite friction at zero load. This offset is drastically enhanced for the Kirigami patterns under strain. Due to the small changes in friction compared to the noise in the data, it is not sensible to calculate the slope  $dF_{\text{fric}}/dF_N$  as a function of load. Nonetheless, if we force a linear fit for the whole range and use the second definition ?? as  $\langle \mu_2 \rangle = \Delta F_{\text{fric}}/\Delta F_N$ , we get average coefficients in the range

$$\mu_2, \text{ ??}: \quad \text{No cut} \sim [4, 9] \times 10^{-5}, \quad \text{Tetrahedron} \sim 5 \times [10^{-5}, 10^{-4}], \quad \text{Honeycomb} \sim [1, 9] \times 10^{-4},$$

depending on the strain values. These numbers should be interpreted cautiously, but we can take it as a rough estimate of the friction coefficient being on the order  $10^{-4}$ – $10^{-5}$ . This relates to the finding by [38] who reported a seemingly non-existing relationship between friction and normal load for a graphene sheet with changes in friction that corresponds to friction coefficients in the range of  $10^{-3}$ – $10^{-4}$  when using the slope definition ??. This supports the idea that the graphene sheet exhibits superlubric behavior in these conditions and that the initial non-strained sheet is in an incommensurable phase. Thus any strain-induced effects might introduce a more commensurable phase that aligns with the observed increase in friction and the fact that the friction never gets smaller than the initial friction value. The non-monotonic increase in friction can then be attributed to transitions in and out of commensurable phases. We found that these strain-induced effects on friction are generally separate from the dependence to load. That is, the introduction of strain mainly shifts the friction-load curve but does not significantly alter its slope.



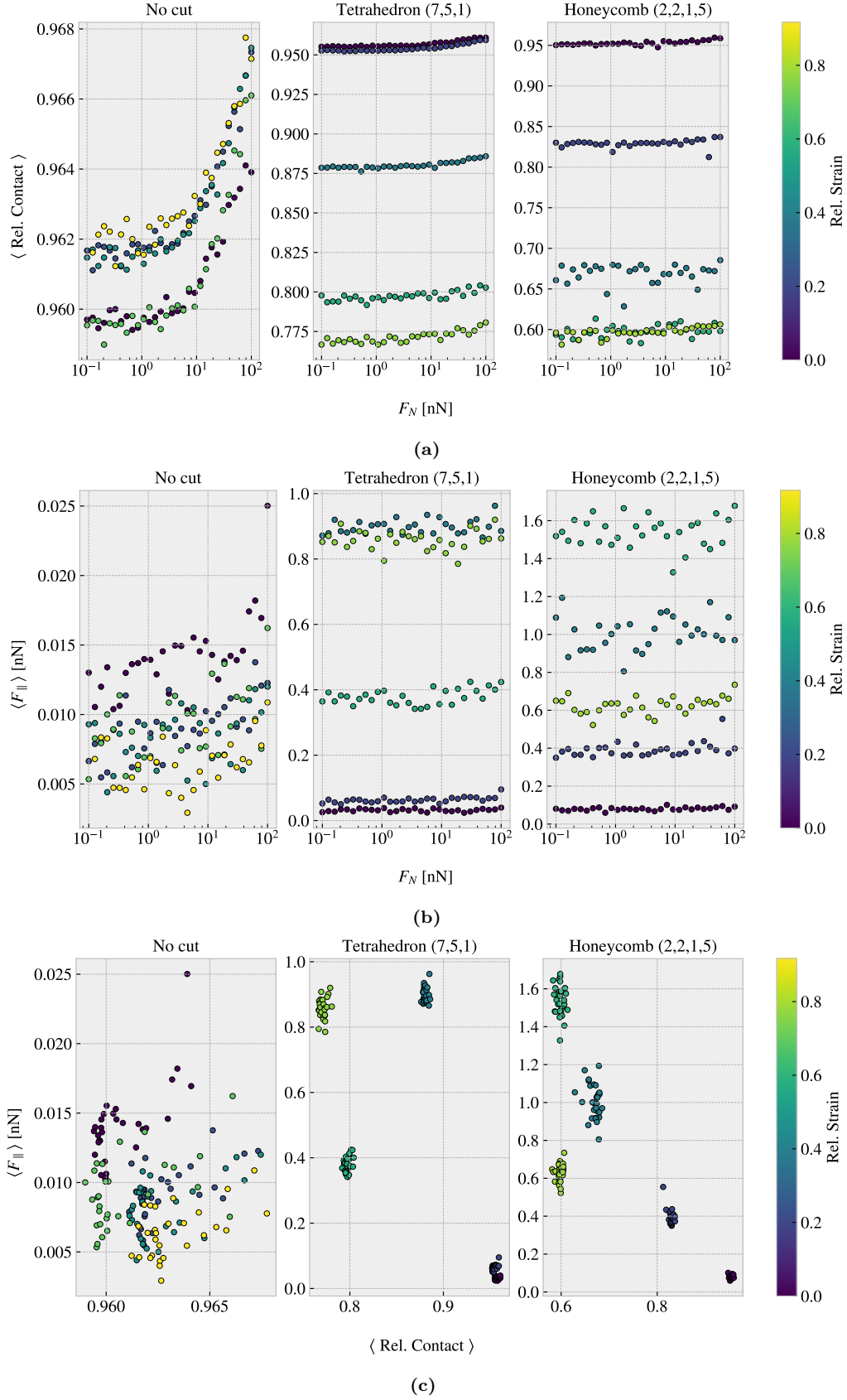


**Figure 2.14:** Investigation of the frictional behavior for the non-cut, Tetrahedron (7, 5, 1) and Honeycomb (2, 2, 1, 5) sheet under varying load, consisting of 30 logarithmically spaced load values in the range 0.1–100 nN, at different strain stages relative to their rupture strains. We omitted the indication of the absolute errors as they were similarly low as seen in Fig. 2.12. (a) The average relative contact vs. load. (b) The average mean friction vs. load. (c) The average mean friction vs. the average relative contact.

### 2.6.4 Prospects for achieving a negative friction coefficient

Considering the results from Sec. 2.6.2 and Sec. 2.6.3 we find that strain-induced friction effects, on the order of 1 nN, are generally dominating in comparison to load-induced effects on the order of 0.01 nN given a load range of 0.1–100 nN. This is promising for the idea of achieving a negative friction coefficient for a nanomachine system that couples load and strain. By applying load on the nanomachine we would increase both the load and the strain on the sheet simultaneously. However, since the friction dependency to strain dominates in comparison to load effects such a system can in practice be designed entirely by considering the strain dependency. The friction coefficient is by our definition (??) given as the slope of the friction  $F_{\text{fric}}$  vs. normal force  $F_N$  curve. Hence, for two points  $\{(F_{N,1}, F_{\text{fric},1}), (F_{N,2}, F_{\text{fric},2})\}$ ,  $F_{N,1} < F_{N,2}$  we can evaluate the associated friction coefficient  $\mu_{1,2}$  as

$$\mu_{1,2} = \frac{F_{\text{fric},2} - F_{\text{fric},1}}{F_{N,2} - F_{N,1}} = \frac{\Delta F_{\text{fric}}}{\Delta F_N}.$$

If we neglect load effects,  $F_{\text{fric}}(F_N, \varepsilon) \sim F_{\text{fric}}(\varepsilon)$ , and consider a load-strain coupling  $\varepsilon = RF_N$  with linear coupling ratio  $R$  we get

$$\mu_{1,2}(\varepsilon_1, \varepsilon_2) = \frac{\Delta F_{\text{fric}}(\varepsilon_1, \varepsilon_2)}{\frac{1}{R}(\varepsilon_2 - \varepsilon_1)} = R \frac{\Delta F_{\text{fric}}(\varepsilon_1, \varepsilon_2)}{\Delta \varepsilon}. \quad (2.1)$$

When considering the ratios  $\Delta F_{\text{fric}}/\Delta \varepsilon$  for the reduction in friction with strain for the Tetrahedron and Honeycomb patterns in Sec. 2.6.2 we find the corresponding coupled system friction coefficients to be

$$\text{Tetrahedron: } R \frac{-0.51 \text{ nN}}{0.04} = -R \cdot 12.75 \text{ nN}, \quad \text{Honeycomb: } R \frac{-0.98 \text{ nN}}{0.36} = -R \cdot 2.72 \text{ nN}. \quad (2.2)$$

This showcases that we might be able to utilize the strain effect to achieve a negative friction coefficient for the system of coupled load and strain. This hypothesis is further investigated in ??.





# Appendices



# Bibliography

- [1] E. Gnecco and E. Meyer, *Elements of friction theory and nanotribology* (Cambridge University Press, 2015).
- [2] Bhusnan, “Introduction”, in *Introduction to tribology* (John Wiley & Sons, Ltd, 2013) Chap. 1.
- [3] H.-J. Kim and D.-E. Kim, “Nano-scale friction: a review”, *International Journal of Precision Engineering and Manufacturing* **10**, 141–151 (2009).
- [4] K. Holmberg and A. Erdemir, “Influence of tribology on global energy consumption, costs and emissions”, *Friction* **5**, 263–284 (2017).
- [5] B. Bhushan, “Gecko feet: natural hairy attachment systems for smart adhesion – mechanism, modeling and development of bio-inspired materials”, in *Nanotribology and nanomechanics: an introduction* (Springer Berlin Heidelberg, Berlin, Heidelberg, 2008), pp. 1073–1134.
- [6] P. Z. Hanakata, E. D. Cubuk, D. K. Campbell, and H. S. Park, “Accelerated search and design of stretchable graphene kirigami using machine learning”, *Phys. Rev. Lett.* **121**, 255304 (2018).
- [7] P. Z. Hanakata, E. D. Cubuk, D. K. Campbell, and H. S. Park, “Forward and inverse design of kirigami via supervised autoencoder”, *Phys. Rev. Res.* **2**, 042006 (2020).
- [8] L.-K. Wan, Y.-X. Xue, J.-W. Jiang, and H. S. Park, “Machine learning accelerated search of the strongest graphene/h-bn interface with designed fracture properties”, *Journal of Applied Physics* **133**, 024302 (2023).
- [9] Y. Mao, Q. He, and X. Zhao, “Designing complex architected materials with generative adversarial networks”, *Science Advances* **6**, eaaz4169 (2020).
- [10] Z. Yang, C.-H. Yu, and M. J. Buehler, “Deep learning model to predict complex stress and strain fields in hierarchical composites”, *Science Advances* **7**, eabd7416 (2021).
- [11] A. E. Forte, P. Z. Hanakata, L. Jin, E. Zari, A. Zareei, M. C. Fernandes, L. Sumner, J. Alvarez, and K. Bertoldi, “Inverse design of inflatable soft membranes through machine learning”, *Advanced Functional Materials* **32**, 2111610 (2022).
- [12] S. Chen, J. Chen, X. Zhang, Z.-Y. Li, and J. Li, “Kirigami/origami: unfolding the new regime of advanced 3D microfabrication/nanofabrication with “folding””, *Light: Science & Applications* **9**, 75 (2020).
- [13] OpenAI, *Dall-e2*, (2023) <https://openai.com/product/dall-e-2>.
- [14] Midjourney, *Midjourney*, (2023) <https://www.midjourney.com>.
- [15] Z. Deng, A. Smolyanitsky, Q. Li, X.-Q. Feng, and R. J. Cannara, “Adhesion-dependent negative friction coefficient on chemically modified graphite at the nanoscale”, *Nature Materials* **11**, 1032–1037 (2012).
- [16] B. Liu, J. Wang, S. Zhao, C. Qu, Y. Liu, L. Ma, Z. Zhang, K. Liu, Q. Zheng, and M. Ma, “Negative friction coefficient in microscale graphite/mica layered heterojunctions”, *Science Advances* **6**, eaaz6787 (2020).
- [17] D. Mandelli, W. Ouyang, O. Hod, and M. Urbakh, “Negative friction coefficients in superlubric graphite-hexagonal boron nitride heterojunctions”, *Phys. Rev. Lett.* **122**, 076102 (2019).
- [18] R. W. Liefferink, B. Weber, C. Coulais, and D. Bonn, “Geometric control of sliding friction”, *Extreme Mechanics Letters* **49**, 101475 (2021).
- [19] M. Metzsch, *Github repository*, <https://github.com/mikkelme/MastersThesis>.

- [20] A. P. Thompson, H. M. Aktulga, R. Berger, D. S. Bolintineanu, W. M. Brown, P. S. Crozier, P. J. in 't Veld, A. Kohlmeyer, S. G. Moore, T. D. Nguyen, R. Shan, M. J. Stevens, J. Tranchida, C. Trott, and S. J. Plimpton, "LAMMPS - a flexible simulation tool for particle-based materials modeling at the atomic, meso, and continuum scales", *Comp. Phys. Comm.* **271**, 108171 (2022).
- [21] E. M. Nordhagen, *LAMMPS simulator*, <https://github.com/evenmn/lammps-simulator>.
- [22] A. H. Larsen, J. J. Mortensen, J. Blomqvist, I. E. Castelli, R. Christensen, M. Dułak, J. Friis, M. N. Groves, B. Hammer, C. Hargus, E. D. Hermes, P. C. Jennings, P. B. Jensen, J. Kermode, J. R. Kitchin, E. L. Kolsbjerg, J. Kubal, K. Kaasbjerg, S. Lysgaard, J. B. Maronsson, T. Maxson, T. Olsen, L. Pastewka, A. Peterson, C. Rostgaard, J. Schiøtz, O. Schütt, M. Strange, K. S. Thygesen, T. Vegge, L. Vilhelmsen, M. Walter, Z. Zeng, and K. W. Jacobsen, "The atomic simulation environment—a python library for working with atoms", *Journal of Physics: Condensed Matter* **29**, 273002 (2017).
- [23] A. Paszke, S. Gross, F. Massa, A. Lerer, J. Bradbury, G. Chanan, T. Killeen, Z. Lin, N. Gimelshein, L. Antiga, A. Desmaison, A. Kopf, E. Yang, Z. DeVito, M. Raison, A. Tejani, S. Chilamkurthy, B. Steiner, L. Fang, J. Bai, and S. Chintala, "Pytorch: an imperative style, high-performance deep learning library", in *Advances in neural information processing systems 32* (Curran Associates, Inc., 2019), pp. 8024–8035.
- [24] S. Li, Q. Li, R. W. Carpick, P. Gumbsch, X. Z. Liu, X. Ding, J. Sun, and J. Li, "The evolving quality of frictional contact with graphene", *Nature* **539**, Number: 7630, 541–545 (2016).
- [25] H. M. Yoon, Y. Jung, S. C. Jun, S. Kondaraju, and J. S. Lee, "Molecular dynamics simulations of nanoscale and sub-nanoscale friction behavior between graphene and a silicon tip: analysis of tip apex motion.", *Nanoscale* **7** 14, 6295–303 (2015).
- [26] Y. Liu, F. Grey, and Q. Zheng, "The high-speed sliding friction of graphene and novel routes to persistent superlubricity", *Scientific Reports* **4**, 4875 (2014).
- [27] P. Zhu and R. Li, "Study of nanoscale friction behaviors of graphene on gold substrates using molecular dynamics", *Nanoscale Research Letters* **13**, 34 (2018).
- [28] J. Zhang, E. Oslob, F. Siddiqui, W. Zhang, T. Ragab, and C. Basaran, "Anisotropy of graphene nanoflake diamond interface frictional properties", *Materials* **12**, 10.3390/ma12091425 (2019).
- [29] F. Bonelli, N. Manini, E. Cadelano, and L. Colombo, "Atomistic simulations of the sliding friction of graphene flakes", *The European Physical Journal B* **70**, 449–459 (2009).
- [30] S. Zhang, Y. Hou, S. Li, L. Liu, Z. Zhang, X.-Q. Feng, and Q. Li, "Tuning friction to a superlubric state via in-plane straining", *Proceedings of the National Academy of Sciences* **116**, Publisher: Proceedings of the National Academy of Sciences, 24452–24456 (2019).
- [31] J. H. Dieterich, "Time-dependent friction in rocks", *Journal of Geophysical Research (1896-1977)* **77**, 3690–3697 (1972).
- [32] R. Guerra, U. Tartaglino, A. Vanossi, and E. Tosatti, "Ballistic nanofriction", *Nature Materials* **9**, 634–637 (2010).
- [33] J. Norell, A. Fasolino, and A. Wijn, "Emergent friction in two-dimensional frenkel-kontorova models", *Physical Review E* **94**, 10.1103/PhysRevE.94.023001 (2016).
- [34] H. Tomaç, Z. Guchan, and N. Altun, "How the stiletto heeled shoes which are popularly preferred by many women affect balance and functional skills?", *Health Care for Women International* **43**, 1–11 (2020).
- [35] K. Gibbs, *Pressure*, (2020) [https://www.schoolphysics.co.uk/age16-19/Mechanics/Statics/text/Pressure\\_/index.html](https://www.schoolphysics.co.uk/age16-19/Mechanics/Statics/text/Pressure_/index.html).
- [36] F. B. Ltd, *Foot facts*, (2023) <https://www.footbionics.com/Patients/Foot+Facts.html>.
- [37] H.-J. Kim and D.-E. Kim, "Molecular dynamics simulation of atomic-scale frictional behavior of corrugated nano-structured surfaces", *Nanoscale* **4**, 3937–3944 (2012).
- [38] M. Dienwiebel, N. Pradeep, G. S. Verhoeven, H. W. Zandbergen, and J. W. Frenken, "Model experiments of superlubricity of graphite", *Surface Science* **576**, 197–211 (2005).